

Decades of Change: Warming Trends and Hydrographic Variability of Atlantic Water as observed in the West Spitsbergen Current (1997–2024)

Rebecca McPherson^{1*}, Wilken-Jon von Appen¹, Laura de Steur², Torsten Kanzow¹, Agnieszka Beszczynska-Möller³, Angelika H. H. Renner⁴

¹ Alfred Wegener Institute, Helmholtz Centre for Polar and Marine Research; Bremerhaven, Germany

² Norwegian Polar Institute; Tromsø, Norway

³ Institute of Oceanology, Polish Academy of Sciences; Sopot, Poland

⁴ Institute of Marine Research, Tromsø, Norway

Abstract

Fram Strait is the main gateway between the Arctic Ocean and the North Atlantic, where warm, saline Atlantic Water (AW) flows northward via the West Spitsbergen Current (WSC) - the main source of oceanic heat and salt entering the Arctic Ocean. An array of moorings has continuously monitored the year-round inflow of AW in the WSC from 1997 to 2024, providing a 27-year record of hydrographic and current measurements. A robust, long-term AW warming trend of 0.20°C per decade was identified, amounting to a total increase of 0.54°C over the observational period. Distinct multi-annual warm and cold anomalies were identified, typically lasting ~2 years. Two warm periods (2005–2007 and 2015–2017) and two cold periods (1997–1999 and 2019–2024) are linked to distinct shifts in the AW temperature regime. These anomalies were generally accompanied by salinity changes, with warm periods associated with more saline conditions and cold periods with fresher waters. The most recent cold anomaly is notable for persisting for over five years - more than twice as long as previous events. Interannual variability in AW temperatures reflects a combination of upstream advection of anomalies from the Nordic Seas and modulation by local atmospheric forcing. These temperature anomalies are advected into the Eurasian Basin and influence downstream conditions. The expected continued AW warming and associated increase in

ocean heat transport will have profound and lasting implications for the physical and ecological future state of the Arctic Ocean.

1. Introduction

Fram Strait, located between Svalbard and Greenland, is the primary gateway connecting the Arctic Ocean and the North Atlantic, facilitating the exchange of heat and freshwater between these two regions. Along the eastern side of the strait, relatively warm and saline Atlantic Water (AW) is carried northwards by the West Spitsbergen Current (WSC) into the Arctic Ocean (Aagaard et al., 1987). On its western side, the southward-flowing East Greenland Current (EGC) advects cold, fresh Polar Water (PW), sea ice, and AW at depth along the Greenland continental shelf edge (Aagaard and Carmack, 1989) (Fig. 1). The WSC is the major source of oceanic heat and salt to the Arctic Ocean (Boyd and D'Asaro, 1994), and variations in the AW inflow strongly influence both Arctic ocean and sea ice conditions (Polyakov et al., 2017; Docquier et al., 2021).

The AW in the WSC originates in the North Atlantic and travels northward along two main branches of the Norwegian Atlantic Current (Holliday et al., 2008; Orvik and Niiler, 2002) (Fig. 1). The eastern branch, the Norwegian Atlantic Slope Current (NwASC), is largely barotropic and follows the continental shelf break (Orvik and Niiler, 2002; Skagseth et al., 2004). Near the Barents Sea, the NwASC bifurcates; part of it flows eastward through the Barents Sea Opening, while the other continues northward into Fram Strait, ultimately forming the narrow core of the WSC. The western branch, the Norwegian Atlantic Front Current (NwAFC), is baroclinic and follows topographic ridges in the central Norwegian Sea (Orvik and Niiler, 2002). This branch also partially reaches Fram Strait and augments the WSC, forming its offshore branch. Approximately half of the AW in the WSC continues into the Central Arctic Ocean, while the remainder recirculates westwards across Fram Strait (Quadfasel et al., 1987; Marnela et al., 2013; Hofmann et al., 2021). This recirculation, mainly fed by the offshore branch, returns southward, subducted beneath the EGC (Quadfasel et al., 1987; Schauer et al., 2004), with part of it driven onto the Northeast Greenland continental shelf. There, the AW can reach the marine-terminating glaciers, meaning that the variability of the AW temperature in the WSC can also impact glacier melting and retreat (Straneo et al., 2012; Straneo and Heimbach, 2013; McPherson et al., 2023; 2024; Wekerle et al., 2024).

The WSC exhibits strong seasonality. In winter, enhanced wind stress over the Nordic Seas intensifies the gyre circulation (Isachsen et al., 2003; Voet et al., 2010), resulting in stronger northwards velocities. As a result, winter volume transports can be twice those of summer (Beszczynska-Möller et al., 2012; Tsubouchi et al., 2023). This seasonal strengthening of the WSC also increases horizontal shear and baroclinic instability, leading to enhanced eddy kinetic energy in the WSC (and central Fram Strait) during winter months (von Appen et al., 2016). These eddies, along with submesoscale processes, are also believed to facilitate the subduction of AW beneath the sea ice and PW carried southward in the EGC (Hattermann et al., 2016).

In recent decades, AW temperatures have increased in Fram Strait, the Nordic Seas, and the Arctic Ocean (Beszczynska-Möller et al., 2012; Muilwijk et al., 2018; Polyakov et al., 2023, 2017; Rudels et al., 2000; Schauer et al., 2008; Tsubouchi et al., 2021). From the 1970s to early 2000s, maximum core AW temperatures rose by 1–2 standard deviations above their annual variability, with a decadal mean temperature anomaly of $+0.9 \pm 0.25^\circ\text{C}$ (Polyakov et al., 2012). This warming extends below the upper ocean and has been recorded at depth in Fram Strait (von Appen et al., 2015; Karam et al., 2024). Arctic amplification appears even stronger than previously expected; near-surface air temperatures have warmed nearly four times faster than the global average over the last four decades (Rantanen et al., 2022; Shu et al., 2022). This warming, attributed in part to global warming (Banks et al., 2000; Barnett et al., 2005; Kay et al., 2011; Kim and An, 2024; Polyakov et al., 2010) is predicted to continue, with lasting consequences for the Arctic Ocean.

To monitor the year-round oceanic exchange of heat, freshwater and sea ice, the Alfred Wegener Institute, Helmholtz Centre for Polar and Marine Research (AWI), and the Norwegian Polar Institute (NPI) have been maintaining a mooring array across Fram Strait since 1997. The array provides hydrographic and current data from both the WSC (AWI) and EGC (NPI). In September 2002, the EGC moorings (all west of the prime meridian) were moved south from 79° N to $78^\circ50'\text{ N}$ to align with the moorings in central Fram Strait (de Steur et al., 2014). In July 2016, the AWI moorings in the eastern part of the strait were relocated northward from $78^\circ50'\text{N}$ to 79°N . At the same time, the moorings monitoring central Fram Strait and the recirculation (4°E to 2°W) were discontinued by AWI given resource constraints, focusing efforts on the WSC. However, NPI has been maintaining a mooring at 2°W since 2018.

In this study, we present 27 years (1997 - 2024) of hydrographic and velocity observations from the Fram Strait mooring array east of 4°E . These data allow a comprehensive update of

the structure and variability of the WSC, building on the last publication that applied this kind of analysis to the observations up to 2010 (Beszczynska-Möller et al., 2012). Section 2 describes the mooring array and how the data were processed and gridded. Section 3 addresses the impact of the northwards relocation of the mooring array in July 2016. The mean structure of the WSC is also confirmed and the seasonal-to-decadal variability of the AW temperature and salinity, in both the offshore and core branches of the boundary current, are described. The drivers of variability are also explored. Section 4 explores the downstream propagation of AW temperature anomalies into the Eurasian Basin, and historical temperature records (1969 – 1997) are used to place the recent warming in a longer-term context, comparing trends over the last five decades. The focus of this study is a subset of questions based on the temperature measurements that one can attain from the mooring array; future work will address the changes in volume transport of the WSC.

2. Data and Methods

2.1. Temperature, salinity, and velocity from WSC moorings

Since 1997, a mooring array measuring velocity, temperature, and salinity year-round has been maintained across Fram Strait, covering the region from the shelf west of Svalbard to the eastern Greenland shelf. The easternmost part of this array (Fig. 1) has been maintained by AWI. From August 1997 to July 2016, the moorings F1 - F7 were deployed along a zonal section at 78° 50'N (Fig. 2a). In July 2016, the array was relocated northwards to 79°N, and the horizontal extent was reduced. The revised configuration comprises, from west to east, HG-IV (referred to here as F6 for ease of nomenclature), F5, F4, F3, F2, F1. The relocation aimed to maintain the moorings approximately along the same isobath to continue to capture a similar current structure of the WSC.

Following [Beszczynska-Möller et al., \(2012\)](#), moorings F1 - F3 span the core of the WSC, and F4 - F5 represent the offshore branch. Due to the increased instrumentation in the near-surface after 2016 (Supplementary Figure 1), F2 and F4 are used as representative of the WSC core and the offshore branch, respectively, when examining the impact of the 2016 northwards shift of the mooring array (Section 3.1).

The mooring configuration evolved since the initial deployment, with a growing number of instruments over time. All moorings measured temperature and velocity at five standard depths: subsurface (75 m); within the AW layer (250 m); near the AW lower boundary (750 m); the deep water (1500 m, where available); and near-bottom (~ 10 m above the bottom;

the deepest mooring was in ~ 2500m depth). In 2016, additional instruments were added in the upper 500 m of F2 - F6 to better resolve near-surface stratification. The AW layer is defined here as the depth range where temperature > 2°C.

Each mooring was equipped with temperature sensors (SBE56, SBE37 and SBE16, Sea-Bird Electronics Inc.) and current metres (RCM7, RCM8, RCM11, Aanderaa Instruments). Many of the earlier temperature measurements were derived from the RCMs. From 2012 onwards, several moorings were also equipped with additional salinity sensors (SBE37) and acoustic doppler current profilers (ADCP) to measure the vertical flow structure in the upper 250 m (RDI 150 kHz QuarterMaster Workhorse ADCP, RD Instruments) or 400 m (RDI 75 kHz Longranger ADCP, RD Instruments) with high resolution. The standard pre-cruise calibration was applied to all of the sensors. Note that the data quality, particularly for the velocity measurements, has improved over the observational period.

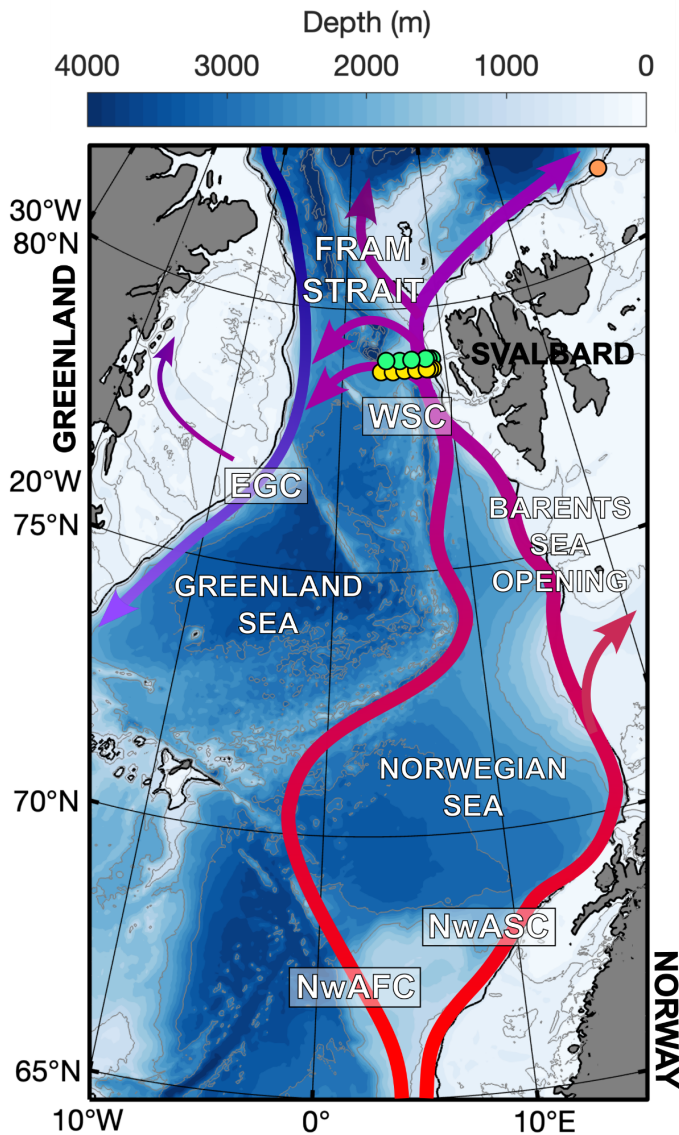


Figure 1. Circulation of Atlantic Water (AW) in the Nordic Seas and Fram Strait. Red arrows indicate the northwards flow of warm, saline AW of the Norwegian Atlantic Slope Current (NwASC) and Norwegian Atlantic Front Current (NwAFC) from the northern North Atlantic to the Barents Sea Opening and the West Spitsbergen Current (WSC) in Fram Strait. The blue arrow indicates the cold and fresh Arctic outflow which joins the East Greenland Current (EGC). The mooring locations across the WSC are marked as circles, at their pre-2016 location at 78° 50'N (yellow), and post-2016 location at 79°N (green). The A-TWAIN mooring in the Svalbard Branch of the AW inflow is marked at 31°E (orange).

2.2. Historical WSC data from moorings and CTD profiles

Prior to the first deployment by AWI of the WSC moorings in 1997 (Fig. 1), direct hydrographic measurements have been collected in Fram Strait since 1969. Between 1971 and 1987, year-round moorings equipped with temperature sensors and current meters were deployed along 79°N, as detailed in Jónsson and Foldvik (1992). From these historical deployments, only moorings within 50 km of the modern F3 and F4 sites were included here. For each, temperatures from the upper 300 m were averaged to obtain an annual mean. The raw data are unavailable and Jónsson and Foldvik (1992) provided only mean temperatures over their respective deployment periods (typically between 306 - 413 days) and their start dates. To obtain a consistent annual mean (365-day) record, a weighted correction was applied based on the mean seasonal cycle of AW temperature (Fig. 9b), accounting for any months missing or duplicated within the original records.

Annual CTD surveys conducted between 1969 to 1997, as described in Saloranta and Haugan (2001), further supplemented these mooring records (Supplementary Table 4). The CTD profiles were averaged over the onshore branch of the WSC, defined as the region spanning the 300 - 1200 m isobaths and latitudes from 78° 50'N – 79° 30'N. Temperatures were averaged between 100 - 300 m depth. As the CTD surveys were typically collected between August and October, a correction was applied to account for the seasonal warm bias. This offset, derived from the seasonal cycle of AW temperature observed in the AWI WSC moorings (1997–2024) (Fig. 9b), involved subtracting 0.6°C to account for the difference between the summer and annual means.

Although these earlier historical measurements carry inherent uncertainties, combining them with the more recent mooring records enables an assessment of long-term changes and trends in AW temperature over the past 56 years.

2.3. A-TWAIN Mooring Data

To examine the downstream advection of the AW inflow from Fram Strait, two moorings maintained by NPI have been deployed north of Svalbard (81.5°N, 31°E, Fig. 1) since 2012. These moorings are located across the Svalbard branch of the AW boundary current as part of the project '*Long-term variability and trends in the AW inflow region*' (A-TWAIN). The moorings were located at the 200-m and 800-m isobaths, covering the upper continental shelf and slope, respectively. Both moorings were equipped with temperature and conductivity sensors as well as current meters.

The shelf break mooring (200 m) was first deployed in September 2012, and provided data from 2012 to 2019, and again from 2021 to 2022. Data is missing for the intervening years due to mooring loss. The slope mooring (800 m), which captures the core of the AW inflow (Pérez-Hernández et al., 2019), recorded data from 2012–2015 and then 2019 - 2020, with gaps similarly due to mooring losses. A comprehensive overview of the moorings and instrumentation for each deployment is provided by Lundsgaard et al., (2021).

The AW temperature timeseries from A-TWAIN presented in Figure 12 is based on the maximum recorded temperature at each mooring site, initially averaged hourly and then monthly. Annual means are calculated as winter-centred averages (September - August), to align with the typical deployment cycle and accounting for the ~2-month advection time of the AW inflow from the WSC in Fram Strait.

2.4. Satellite Sea Surface Temperature Data

Sea surface temperature (SST) was taken from the high-resolution blended product of satellite infrared and microwave observations for the years 1997 - 2024 (NOAA OI SST V2) (Huang et al., 2021). The blending of infrared and microwave data ensures that SST estimates are also available in the presence of clouds. The data were mapped onto a 0.25° x 0.25° global grid at a daily resolution as described in Reynolds et al., (2007), and monthly averaged. The good agreement between upper ocean temperatures from the moorings and SST is demonstrated in Supplementary Figure 3.

2.5. Satellite Altimetry Data

Sea-surface height (SSH) used in this study was obtained from the Copernicus Marine Environment Monitoring Service (CMEMS) multi-mission combined product (E.U. Copernicus Marine Service Information, 2021). The data is globally gridded (0.25° x 0.25°) and has a daily resolution over the time period 1997 - 2024. The L4 product was estimated by optimal

interpolation, merging along-track observations from multiple altimeter missions. Surface geostrophic currents are a product of the altimetry observations. The robustness of using satellite altimetry gridded products to study the variability of sea-level and surface geostrophic currents in the Nordic Seas has been well demonstrated (Volkov and Pujol, 2012). The coverage of the repeated along-track satellite cycles is generally very good over eastern Fram Strait (east of 2°E) as the ice edge is mostly located in the centre of Fram Strait (illustrated in Supplementary Figure 3).

2.6. Sea Ice Concentration

Sea ice concentration is ERA5 reanalysis data provided at an hourly temporal resolution from 1997 - 2024 (Hersbach et al., 2020) from which a monthly mean is calculated. The data is globally gridded ($0.25^\circ \times 0.25^\circ$). Two sea ice products are used in ERA5. From 1997 - 2007, the Global Sea Ice Concentration data record was produced by EUMETSAT's Ocean and Sea Ice Satellite Application Facility (OSI SAF). From September 2007, the OSI SAF operational sea ice product is part of the UK MetOffice Operational Sea Surface Temperature and Sea Ice Analysis (OSTIA).

2.7. Construction of Gridded Fields

Velocity, temperature and salinity were measured at time intervals ranging from 10 minutes to 2 hours. Velocity data were low-pass filtered (40-hour cut-off) to remove tidal signals. All variables were averaged hourly and interpolated onto a regular grid with 4 m vertical spacing. Where pressure sensors were present, measurements were mapped directly to the corresponding depths to account for vertical mooring motion (knockdowns) caused by strong horizontal currents (Supplementary Figure 1). For earlier deployments (up to ~2010), some instruments lacked pressure sensors and were therefore assigned to a fixed nominal depth. In cases where mooring knockdowns occurred during periods of vertical temperature stratification, deeper (e.g., colder) measurements may be incorrectly mapped to a shallower nominal depth. However, this potential cold bias is limited in both magnitude and duration, as strong vertical temperature gradients resulting from surface warming typically persist for only four months each year (Fig. 4c,d), and can be reversed due to the presence of the surface freshwater layer. This potential bias primarily affects the early years of the record (up to 2012) but remains smaller than if the temperature gradient were unidirectional and persistent year-round. This consideration is particularly relevant in the WSC core, where strong inflows can produce knockdowns exceeding 100 m.

Due to occasional instrument and mooring failures, complete records were not available at all standard depths for every mooring location (Supplementary Figure 1). Where data at a

standard depth was missing, it was substituted by reconstructed data (X_R), composed of the sum of three components of the measured timeseries,

$$X_R = X_{\text{mean}} + X_{\text{season}} + X_{\text{trend}}$$

where the long-term mean (X_{mean}), a seasonal cycle (X_{season}) and a linear trend (X_{trend}) were calculated from the measured data at each standard depth. To account for multidecadal variability, the linear trend and mean were calculated separately for three periods, i.e., between 1997 - 2007; 2007 - 2017; and 2017 - 2024. Due to the vertical motions, these components were calculated over a depth range surrounding each standard depth (i.e., 75 ± 25 m; 250 ± 50 m; 750 ± 50 m; 1500 ± 100 m; $2500/\text{bottom} \pm 100$ m). All data was then linearly interpolated vertically from the deepest original measurement to the surface for temperature and velocities where satellites provided surface data, and for salinity, to either the depth of the shallowest measurement of 50m, whichever was shallower. No horizontal interpolation was applied between moorings, as shown in Fig. 3.

Monthly means were calculated for all fields from the gridded hourly data and used in the subsequent analyses. Annual means are defined as winter-centred averages spanning July to June, to align with the typical deployment periods. Note that given the length of the measurement records, the standard error is very small (e.g. $\sim 0.2^\circ\text{C}$). Gridding and reconstruction steps are illustrated in Supplementary Fig. 2. To assess variability across different timescales (e.g., seasonal, interannual), variance associated with each timescale was decomposed by filtering the time series accordingly, computing the standard deviation of the filtered data, and normalising by the total standard deviation of the full monthly-mean time series. This quantifies the proportion of overall variability attributable to each timescale and specific mode of variability.

2.8. Regime Shift Detection

A sequential algorithm for regime shift detection (Rodionov, 2004) was applied to the monthly AW temperatures averaged over both branches of the WSC, after removal of the mean seasonal cycle. The method identifies discontinuities in a time series without requiring prior assumption about their timing. The method first checks each data point's anomaly against the current regime's mean value. If a data point is statistically significant, the subsequent data points are sequentially tested to assess the confidence of the shift. A regime shift index (RSI), defined as the cumulative sum of normalized deviations from the new regime's hypothesized mean, is used to assess statistical significance via a Student's t-test. If the RSI remains positive for all points within a specified cutoff length, the null hypothesis of a constant mean is rejected, indicating a regime shift (Rodionov and Overland, 2005). Similar

approaches have been used to identify shifts in other long-term temperature time series (de Steur et al., 2023; Karam et al., 2024).

A cut-off length of 10 years was used to capture multidecadal variability, although tests with 8- and 12-year cut-off lengths yielded similar results. Before applying the shift detection procedure, the AW temperature time series was normalised using a quantile transform. This transform maps the cumulative density function (CDF) of the original series onto a Gaussian CDF, ensuring the data meet the method's assumption of normally distributed inputs.

3. Results

3.1. Impact of the 2016 relocation of the mooring array from 78°50'N to 79°N

In July 2016, the eastern Fram Strait mooring array covering the WSC was relocated 10 nm (18 km) northward, from 78° 50'N to 79°N (Fig. 1, 2a). The longitudinal positions of the moorings F4 - F6 were also adjusted slightly, though they remained approximately aligned with the same isobaths. To evaluate the impact of this northward relocation, the differences in the long-term mean and variability of velocity and temperature at selected mooring sites are examined. This approach follows that of de Steur et al., (2014), who examined the impact of a similar, but southward, mooring shift in the EGC in 2002.

The three easternmost moorings (F1 - F3), located between 8 and 9°E, are situated above the upper shelf slope and measure the steady northward flow of the WSC core (Fig. 2a). The flow is strongest near the continental shelf edge and has a dominant northwards direction, generally following the isobaths. Near the shelf edge at F2, which represents the WSC core, the mean velocity at 75 m was 0.17 ms^{-1} with a standard deviation of $\pm 0.05 \text{ ms}^{-1}$ at 78° 50'N, and remained comparable at $0.17 \pm 0.07 \text{ ms}^{-1}$ at 79°N. In the AW layer (i.e. at 250 m depth), the velocities were similar: $0.18 \pm 0.04 \text{ ms}^{-1}$ at 78°50'N and $0.18 \pm 0.06 \text{ ms}^{-1}$ at 79°N. The flow weakened with depth towards 750 m, i.e. the AW lower boundary, reaching 0.09 ± 0.02 and $0.09 \pm 0.03 \text{ ms}^{-1}$ at 78°50'N and 79°N respectively. These core velocity magnitudes are consistent with previous studies (e.g., Beszczynska-Möller et al., 2012; Schauer et al., 2008; von Appen et al., 2016).

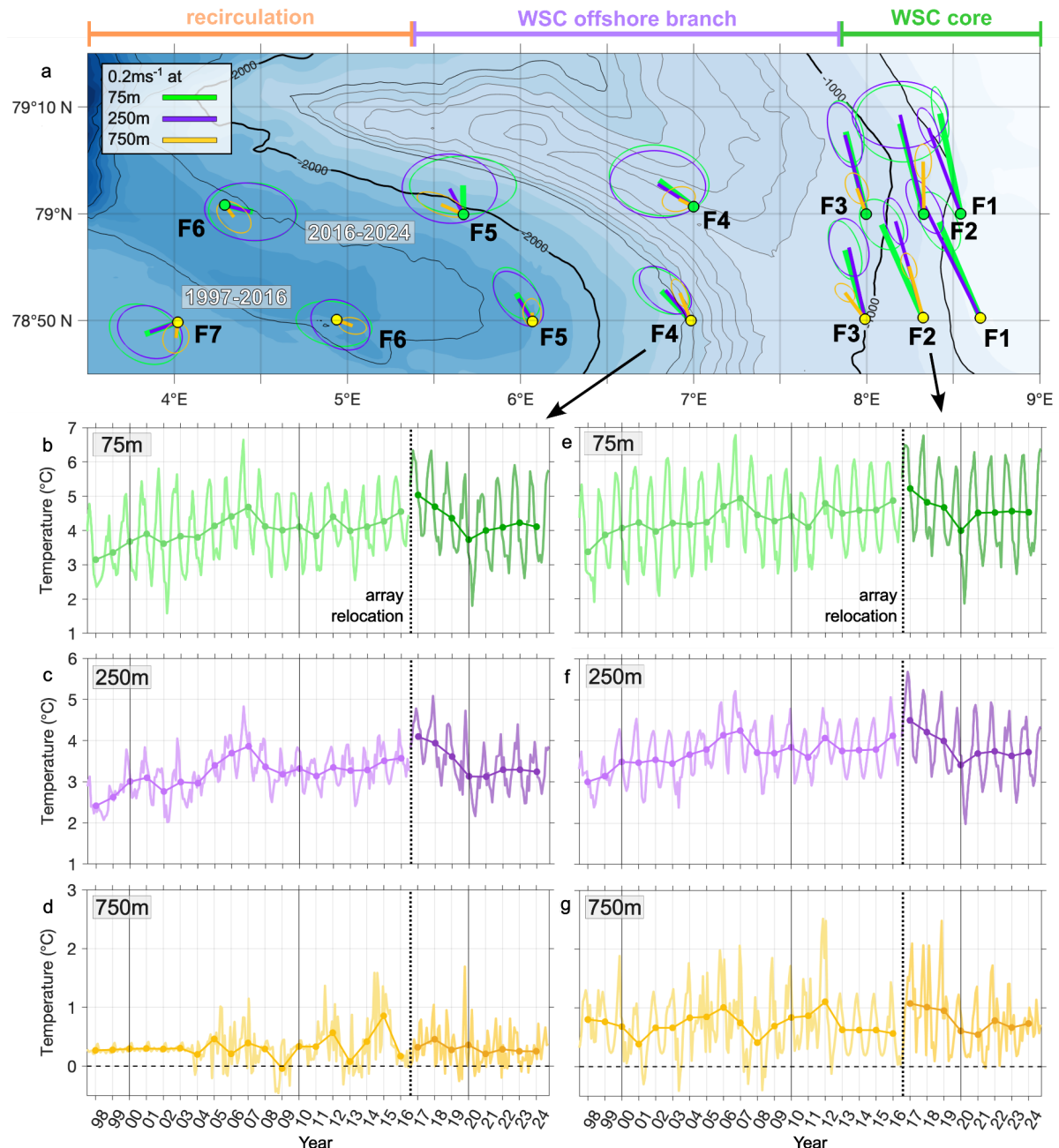


Figure 2: Properties of the WSC at both mooring locations. (a) Mean velocity vectors (lines) and standard deviation ellipses at pre and post-2016 mooring locations (circles) for depths of 75 m (green), 250 m (purple), and 750 m (yellow). Thick black lines show the 1000 m and 2000 m contours. (b - g) Mean potential temperatures at mooring sites F4 (left panels) and F2 (right panels), representing the core and offshore branches of the WSC, respectively, at approximately (b,e) 75 m, (c,f) 250 m, and (d,g) 750 m depth. Monthly means (solid lines) and winter-centred annual means (dotted lines) are shown. Vertical solid lines mark each decade; the vertical dotted line is July 2016, when the mooring array was relocated.

Flow speeds decreased with distance from the shelf edge and became more variable in direction toward central Fram Strait, illustrated by the larger standard deviation ellipses in Fig 2a. Near the base of the continental slope at F4, representing the offshore WSC branch, mean northwards velocities at 75 m were $0.06 \pm 0.04 \text{ ms}^{-1}$ at $78^\circ 50'N$ and $0.05 \pm 0.07 \text{ ms}^{-1}$ at $79^\circ N$. At 250 m, the velocities were $0.06 \pm 0.05 \text{ ms}^{-1}$ and $0.04 \pm 0.06 \text{ ms}^{-1}$ respectively, and at 750 m they decreased slightly to $0.05 \pm 0.03 \text{ ms}^{-1}$ and $0.04 \pm 0.02 \text{ ms}^{-1}$. West of $6^\circ E$, the large standard deviation ellipses at both latitudes indicate that this region is dominated by similar levels of variability (Fig. 2a). This is likely due to strong eddying activity and variability that is driven by recirculating branches that originate from the WSC and advect AW westwards (Quadfasel et al, 1987; von Appen et al, 2016, Hofmann et al., 2021). Overall, the consistent alignment of the mean flow direction and the comparable velocities at both latitudes, remaining within the range defined by the standard deviation, suggests that the 2016 northward relocation had no significant impact on the qualitative structure of the AW velocity field in the WSC.

Next, the vertical temperature structure at $78^\circ 50'N$ and $79^\circ N$ is compared in both the core (F2) and the offshore branch (F4) of the WSC. To account for underlying trends, mean values were calculated over the same number of years before and after the relocation (i.e., 2008–2016 and 2016–2024). At F2, the average near-surface temperature at 75 m was $4.5 \pm 0.9^\circ C$ at $78^\circ 50'N$ and $4.6 \pm 1.1^\circ C$ at $79^\circ N$ (Fig. 2e). At 250 m, temperatures were $3.8 \pm 0.5^\circ C$ and $3.9 \pm 0.8^\circ C$ at $78^\circ 50'N$ and $79^\circ N$, respectively (Fig. 2f). Similar temperature variability is observed at F4: at 75 m, temperatures averaged $4.1 \pm 0.8^\circ C$ at $78^\circ 50'N$ and $4.3 \pm 1.0^\circ C$ at $79^\circ N$ (Fig. 2b), and at 250 m, $3.3 \pm 0.4^\circ C$ and $3.5 \pm 0.6^\circ C$ (Fig. 2c). At 750 m, temperatures generally fell below the $2^\circ C$ that defines AW, with variability slightly higher at F2 than at F4 (Fig. 2d,g). Notably, the initial six years of temperature data at 750 m at F4 (beginning in 2003) are reconstructed (Fig. 2d). The large standard deviations across the depths reflect the strong seasonal and interannual variability that characterises the AW inflow in the WSC. The comparable mean temperature and variability at both latitudes indicate no substantial differences in the qualitative AW temperature structure in either the core or offshore branch of the WSC.

The advective time between $78^\circ 50'N$ and $79^\circ N$ in the WSC core is just over 1 day, based on the 10 nm separation and the average near-surface velocity of 0.18 ms^{-1} at F2 (Supplementary Table. 1). Observations indicate that AW cools by approximately $1^\circ C$ over the ~ 250 km south of the WSC mooring array (Holliday et al., 2008). If this rate of cooling continued northwards, a temperature decrease of $\sim 0.07^\circ C$ would be expected between

78°50'N and 79°N. This estimate is consistent with mooring data from Hofmann et al., (2021), which show a ~0.05°C decrease at 250 m along the prime meridian in central Fram Strait over the same latitude span. Although a stronger gradient of 0.4°C was observed at 50 m depth, these conditions are already more influenced by the EGC and represents an upper bound for the WSC. In any case, this estimated temperature decrease is an order of magnitude smaller than the typical intra- and interannual AW temperature variability at both latitudes, and lies well within the observed standard deviations.

Such a small temperature difference is to be expected, given that most of the AW recirculation occurs between 78°50'N and 79°N and leaves the WSC (Fig. 1), reducing the volume transport while having a minimal impact on the temperature of the WSC core that continues northward. This situation contrasts with the southward relocation of the mooring array in the EGC, where the much warmer recirculating AW significantly warms the colder boundary current between 79°N and 78° 50'N, resulting in notable differences in temperature and volume transport (de Steur et al., 2014).

Taken together, the tight coupling of AW velocity and temperature fields in the WSC, the short advective time between the two latitudes, and limited time for its cooling all indicate that the measurements at 78° 50'N and 79°N reflect a continuous and coherent AW inflow signal in the WSC. Accordingly, the 2016 relocation had no appreciable effect on the qualitative structure of the AW, and the resulting time series across both deployments can be treated as a consistent record.

3.2. Mean structure of the WSC branches

The WSC exhibits a two-branch structure, consistent with Beszczynska-Möller et al., (2012). The core of the WSC is represented by the three easternmost moorings (F1 - F3) above the upper shelf slope, and is characterized by the highest observed temperatures, exceeding 4°C (Fig. 3a), and is distinguishable from the offshore branch (F4 - F5) which carries comparatively cooler AW (Supplementary Table 1). A strong vertical temperature gradient marks the lower boundary of the AW layer (defined as temperature > 2°C) at approximately 500 m depth, extending westwards across the section and into central Fram Strait, west of 4°E (Fig 3a). The WSC core is also associated with a salinity maximum within the upper AW layer above 250 m (Fig. 3b). However, salinity decreases near the continental shelf break, possibly influenced by freshwater input or the less saline Svalbard coastal current. The shorter salinity record at F1 (Supplementary Figure 1) means the robustness of this near-shelf freshening signal warrants caution.

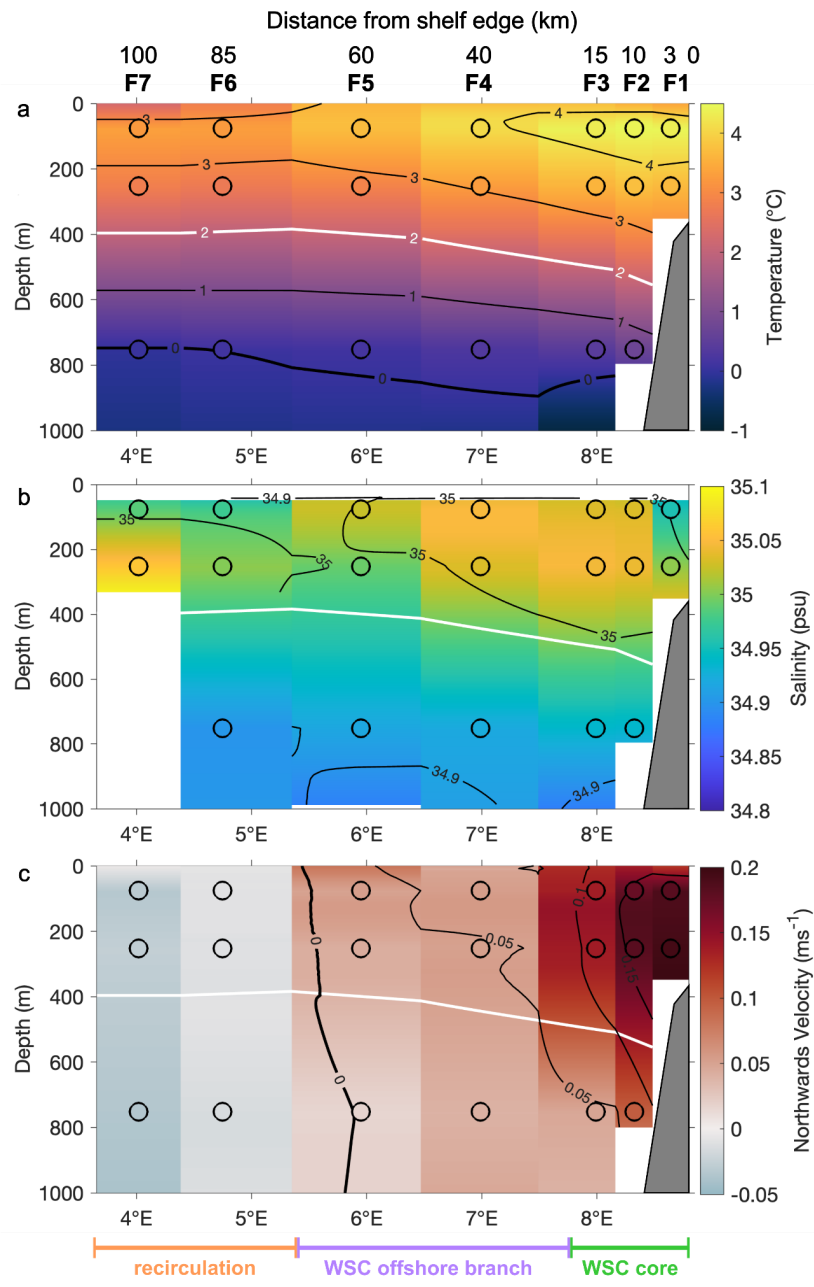


Figure 3: Long-term mean hydrographic and velocity structure of the WSC. Mean (a) potential temperature, (b) salinity, and (c) northwards velocity in the upper 1000 m (50 m – 1000 m for salinity) across the mooring array (labelled F1 - F7). Background colour shows the mean of the vertically interpolated data at each mooring location; coloured circles represent observed means at each of the nominal depths, averaged over the full record (1997 - 2024). Contours show specific isotherms, isohalines and velocity isopleths. The thick white line marks the 2°C isotherm, indicating the AW layer in all panels. In (a) and (c) the thick black contour line marks the 0°C isotherm and 0 ms^{-1} velocity contour respectively. The

grey shading on the right denotes the Svalbard continental shelf. The distance of each mooring from the shelf edge (0km) are labelled at the top of (a).

The velocity structure reinforces the distinction between the WSC core and its offshore branch. The core is predominantly barotropic, with mean northward velocities peaking at 0.2 ms^{-1} along the upper Svalbard continental shelf edge at F1, decreasing to $\sim 0.1 \text{ ms}^{-1}$ at F3 (Fig. 3c, Supplementary Table 2). In contrast, the offshore WSC branch, located east of 5.5°E , is characterised by weaker northwards flow (Fig. 3c). It is clearly separated from the eastern core by the strong horizontal velocity gradient (Fig. 3c), also visible in the mean current vectors (Fig. 2a). These observed temperature and velocity characteristics are consistent with previous estimates of the two WSC branches (Schauer et al., 2008; Beszczynska-Möller et al., 2012; von Appen et al., 2016).

West of the offshore branch, in the central Fram Strait (F6 - F7), the banded structure of southward meridional current components (Fig. 3c) and mean current vectors (Fig. 2a) reflect the presence of eddies and high variability. These features are associated with the recirculating branches of the WSC that transport AW westwards. Schauer et al., (2008) documented the pronounced variability in volume transport at this offshore location, where the flow was steered by the southeastern extension of the Molloy Deep (Fig. 1).

3.3. Seasonal cycle of the WSC branches

The monthly-averaged AW temperatures in both the WSC core and offshore branch exhibit a strong seasonal cycle (Fig 2). In the upper AW layer at 75 m, this seasonal signal accounts for over 70% of the total AW temperature variability in both branches, and remains the dominant source of variability throughout the AW layer down to 250 m. This seasonality is consistent with previous observations of seasonal variability in the WSC (Beszczynska-Möller et al., 2012; von Appen et al., 2016).

The seasonal cycle of temperature shows a clear surface-intensified warming pattern, with a progressive downward propagation of the seasonal thermocline throughout the year in both WSC branches (Fig 4 c,d). During winter and early spring (January–April), temperatures remain relatively uniform throughout the upper 500 m, with the coldest values around 3°C extending downwards from the surface. Between July and September, surface temperatures peak at $\sim 7^\circ\text{C}$, creating a sharp thermocline, while cooler waters persist at depth. This seasonal warming leads to the formation of a shallow summer thermocline, with elevated surface temperatures and strong vertical gradients. While this warm layer remains relatively

shallow, isotherms gradually deepen into the upper AW layer, reaching ~200 m by late summer. This seasonal stratification is subsequently eroded from October onward as surface cooling dominates and heat is redistributed downward, deepening the mixed layer and weakening the summer thermocline. The winter regime is marked by weak near-surface stratification due to intensified atmospheric cooling in the Nordic Seas, where air sea heat fluxes are substantially stronger than in summer (Schlichtholz and Houssais, 2011; von Appen et al., 2016).

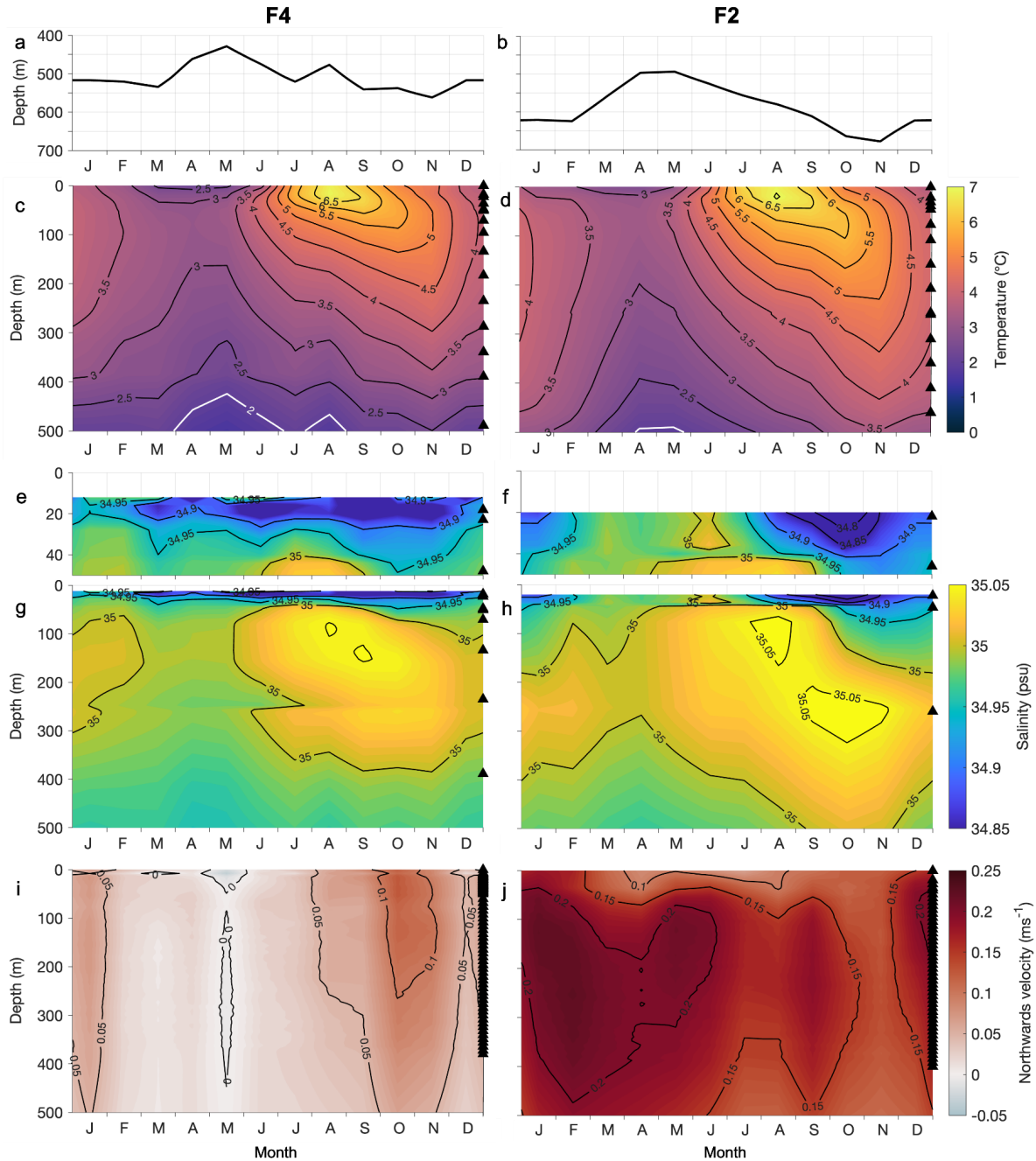


Figure 4. Mean seasonal cycle of AW properties in the two WSC branches. Average seasonal cycle of (a,b) the depth of the AW layer (2°C isotherm), (c,d) potential temperature, (g,h) salinity, (e,f) zoomed view of the upper 50 m of salinity, and (i,j) northwards velocity in the upper 500 m at the offshore branch of the WSC (F4, left) and WSC core (F2, right). Black contours show selected isotherms, isohalines, and velocity isopleths; the 2°C isotherm is highlighted in white in (c) and (d). Triangles at the right edge of each panel indicate the nominal depths of instruments on the respective moorings. This figure is based on monthly averages from July 2016 to July 2024 when there was an increase in the near-surface instrumentation coverage (see Supplementary Figure 1).

In the offshore branch (F4), near-surface salinities are better resolved due to additional instrumentation in the upper 15 m. A persistent low-salinity surface layer (~40 m thick) is present year-round (Fig. 4e). From late spring to early autumn (May to October), a slight freshening in the upper 20 m suggests a seasonal freshwater input, likely due to sea-ice melt. This freshening stabilizes the upper water column and contributes to the formation of a shallow halocline (von Appen et al., 2021). During late autumn and winter (December to March), surface salinities increase, weakening the stratification and indicating enhanced vertical mixing. Although upper-ocean salinity measurements are more limited in the WSC core (Fig. 4f), a similar near-surface seasonal signal is also expected based on near-surface CTD measurements across the width of the WSC (von Appen et al., 2016).

The seasonal deepening of isohalines (Fig. 4g,h) and isotherms (Fig. 4c,d) corresponds to the thickening of the AW layer (i.e. the 2°C isotherm) in summer and autumn. At F2, the AW layer deepens from a minimum of 492 m in May to a maximum of 678 m in November (Fig. 4b). A similar seasonal thickening is observed at F4, where the layer deepens from 428 m to 561 m over the same period (Fig. 4a).

The velocity field also exhibits strong seasonality. In the WSC core, northward flow peaks at $> 0.2 \text{ ms}^{-1}$ during late winter and early spring (February to April) and extends down to the base of the AW layer (Fig. 4j). During summer and autumn, the core of the intensified flow gradually shoals and weakens, with peak velocities confined to shallower depths and decreasing towards 0.1 ms^{-1} . In the offshore branch, peak northwards flow, exceeding 0.1 m s^{-1} , occurs three months earlier, in October - November, and decreases to near-zero by May (Fig. 4i). During this period, the near-surface flow is even slightly southward, indicating a seasonal weakening or even temporary collapse of the offshore branch in summer.

The stronger northwards flow in winter is driven by the intensified wind stress curl over the Nordic Seas which enhances the cyclonic circulation of the Greenland Sea Gyre (Chatterjee et al., 2018). This observed temporal offset in velocities between the two WSC branches reflects their differing sensitivity to this atmospheric forcing: the offshore branch is more closely related to the gyre circulation than the flow near the West Spitsbergen shelf break that forms the WSC core. Additionally, in the offshore branch, the winter-intensified wind forcing drives a shallow northward flow that diminishes rapidly with depth, leading to weak vertical shear throughout the AW layer. In contrast, the WSC core exhibits a subsurface velocity maximum located below ~100 m, with velocities declining toward the surface (Fig. 4j). This pattern likely reflects the influence of the prevailing winter-intensified northerly winds in Fram Strait (Long et al., 2024) which act to counter the northward near-surface flow.

3.4. Interannual variability of the AW in the WSC

The dominant seasonal cycle extends across the width of the mooring array, with warm AW present in both branches of the WSC and in central Fram Strait from late summer and early winter (Fig. 5b). To isolate the interannual variability of the AW temperatures, the influence of the seasonal cycle and long-term trend was removed, followed by the application of a 15-month low-pass filter. The resulting timeseries of AW temperature anomalies is a pattern of positive and negative deviations that extend longitudinally across the width of the array with striking uniformity and persist over many months (Fig. 5c). This horizontal coherence contrasts with the AW seasonal signal, where temperature gradients generally decrease from the WSC core into central Fram Strait (Fig. 5b), suggesting that interannual variability is more spatially coherent and occurs uniformly across the width of the WSC. Consequently, averaging across the array's width at 75 m provides a reliable proxy of AW temperature anomalies (Fig. 5d).

This horizontal coherence is mirrored in the vertical structure of the anomalies. A strong correlation of over 0.95 ($P < 0.05$) between the temperature anomalies at 75 m and 250 m, with comparable amplitudes (not shown), confirms that interannual temperature variability extends throughout the AW layer. This vertical and horizontal uniformity indicates that the mean AW temperature time series - averaged over the array's width and the AW layer depth - effectively captures the variability of the WSC. It also confirms that the post-2016 reduction in the mooring array's spatial extent (Fig. 2a) remains sufficient for monitoring seasonal to decadal variability, including in central Fram Strait.

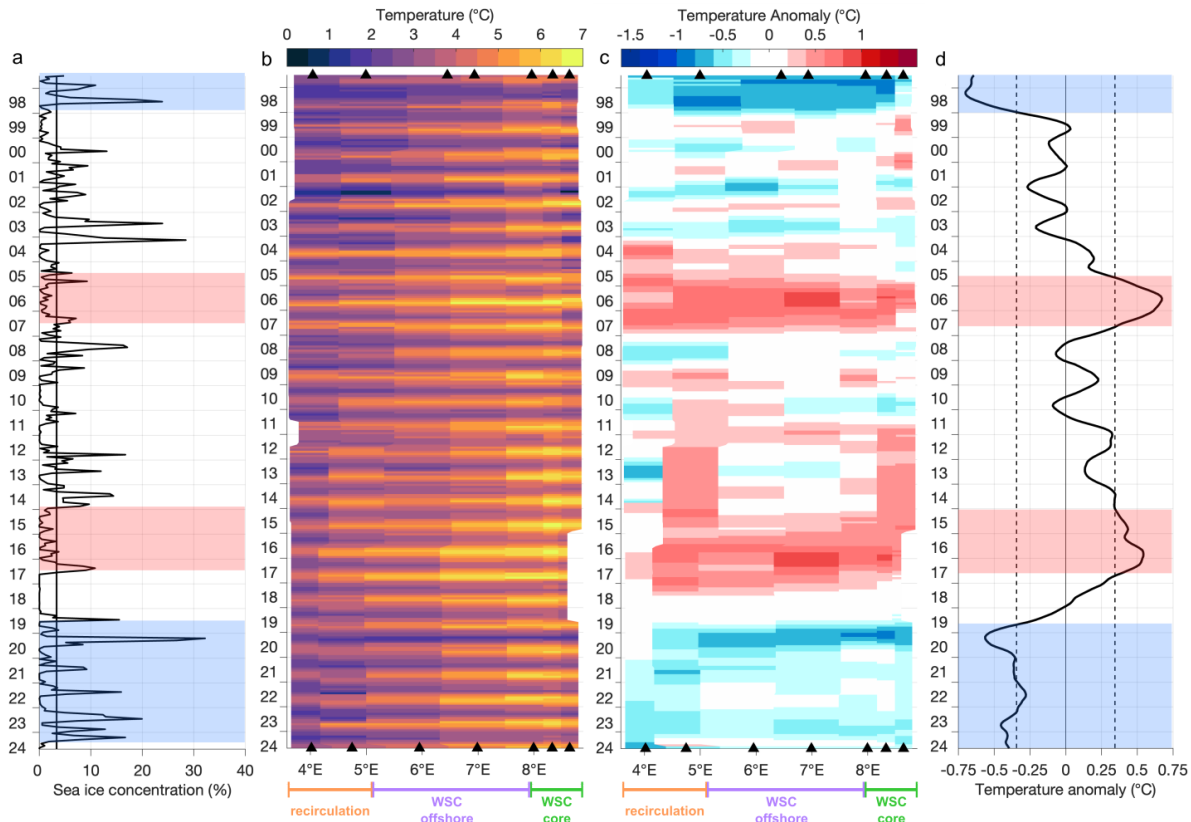


Figure 5. Spatio-temporal variability of AW temperature across eastern Fram Strait.

(a) Monthly average sea ice concentration between 2° - 9°E at 79°N . Hovmöller diagrams at 75 m depth across the WSC mooring array show (b) potential temperature and (c) temperature anomalies after removing the long-term trend and seasonal cycle, and applying a 15-month low-pass filter. (d) The horizontally averaged anomalies from (c), with shaded periods indicating the distinct multi-annual anomalous AW warm (red) and cold (blue) anomalies, defined as deviations exceeding ± 1 standard deviation from the mean (dashed lines). Black triangles in (b) and (c) mark the mooring locations; pre-2016 locations are at the top and post-2016 locations are at the bottom.

Distinct multi-annual AW temperature anomalies were identified by selecting deviations exceeding ± 1 standard deviation from the mean that persist for at least 12 months, after removing the seasonal cycle and long-term trend. Two cold anomalies were recorded: from July 1997 (or earlier, as this was the start of the array) to January 1999, and from September 2019 to July 2024 (or later, as this marks the most recently recovered data). Two warm anomalies occurred from August 2005 to July 2007 (previously identified in Beszczynska-Möller et al., (2012)) and from February 2015 to July 2017 (Fig. 5d). Notably, the second cold AW temperature anomaly persisted for approximately five years - over twice the duration of the other anomalous periods - and did not return to the mean state after 2 - 3 years as observed previously. Although this extended cold period approached the -1

standard deviation threshold, its longevity of strongly negative anomalies suggests a potential shift towards a colder AW mean state, further explored in Section 3.5. These anomalous temperature periods were spatially coherent, stretching across the width of the mooring array (Fig. 5c), with bands even extending into the central Fram Strait and the EGC west of 2°W (Supplementary Figure 3).

The warm AW anomalies coincided with periods of low sea ice concentration in eastern Fram Strait, while the cold anomalies were associated with increased sea ice cover (Fig. 5a). During anomalously warm years, average sea ice concentration between 2°E and 9°E fell below 3%, compared to the peaks above 20% during both cold periods. A significant correlation of -0.5 ($P < 0.05$) between monthly AW temperature anomalies and mean sea ice concentration supports a previously established connection which links warmer AW temperatures and sea ice decline over recent decades in Fram Strait (Wang et al., 2020).

Remarkably, during the second anomalously cold period (2019 - 2024), the peak in sea ice coverage in March 2020 (Fig. 5a) coincided with a notable eastward intrusion of PW (defined as $T < 0^{\circ}\text{C}$) that reached across eastern Fram Strait, through the WSC, and onto the Svalbard continental shelf (Fig. 5b). This intrusion was also evident in the salinity field as a distinct freshwater band at 75 m depth (Fig. 6a), marking the onset of a negative salinity anomaly as much as -0.1 psu between mid-2019 and 2020 across the mooring array (Fig. 6b). In general, the anomalously cold periods are associated with fresher conditions, as seen during the 1997–1998 and 2019–2024 temperature anomalies (Fig 6c,d) while conversely, warm anomalies aligned with positive salinity anomalies from mid-2005 to mid-2007, and again from 2016 to mid-2017. A strong correlation of 0.88 ($P < 0.01$) between the temperature and salinity anomalies suggests a tendency for warm/saline and cold/fresh anomalies to co-occur, though not always concurrently.

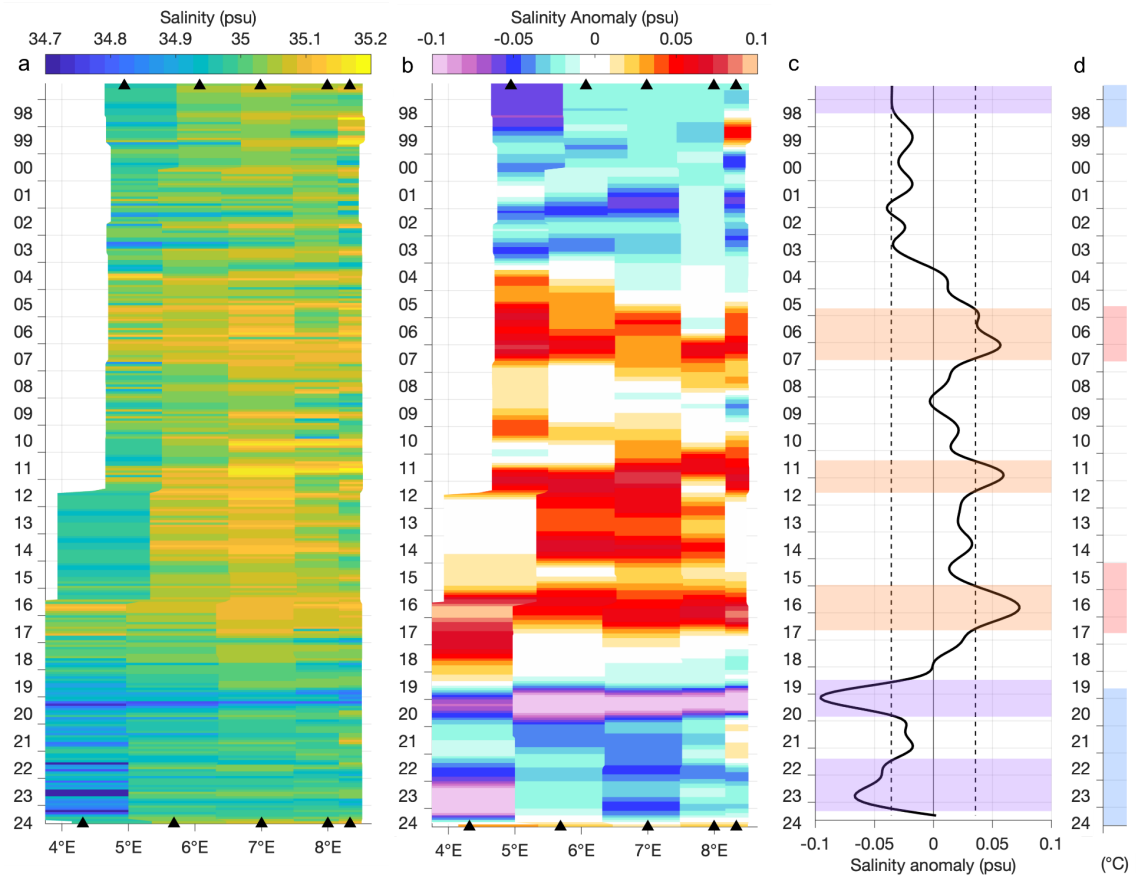


Figure 6. Salinity variability across the WSC. Hovmöller diagrams at 75 m depth across the mooring array (F2 - F6) in eastern Fram Strait show (a) salinity and (b) salinity anomalies, after removing the long-term trend and seasonal cycle and applying a 15-month low-pass filter (1997 - 2024). (c) Mean salinity anomaly from (b), with multi-annual anomalous salty (orange) and fresh (purple) AW periods shaded, defined as anomalies exceeding ± 1 standard deviation from the mean (dashed lines). (d) Warm (red) and cold (blue) AW temperature anomalies from 1997 - 2024, as defined in Fig 5d. Black triangles in (b) and (c) mark the mooring locations; pre-2016 locations are at the top and post-2016 locations are at the bottom.

From July 1997 to 2021, salinity anomalies exhibited minimal lateral gradient across the mooring array (Fig. 6b), reflecting the spatial uniformity seen in the AW temperature anomalies (Fig. 5c). However, after 2021, a notable eastward spread of freshwater anomalies emerged during the summer months, with peak negative salinity anomalies spanning 4 - 5°E and extending into the offshore branch of the WSC - reaching magnitudes more than twice those observed in the WSC core (Fig. 6b). These localized freshwater peaks align with winter/spring increases in sea ice concentration which frequently exceeded 15%, nearly four times the long-term mean (Fig. 5a). This suggests that summer-intensified

freshwater anomalies in the offshore branch may be linked to enhanced meltwater input from the anomalously high sea ice concentrations in central Fram Strait.

3.5. Long-term trends in AW temperature

The 27-year time series enables analysis of multidecadal AW temperature trends in the WSC. Linear fits to the annual mean temperatures of the AW layer ($T > 2^{\circ}\text{C}$) show statistically significant warming trends ($P < 0.05$) across the WSC, though with different rates between the core and offshore branches (Fig. 7). In the WSC core (F1 - F3), AW temperatures increased by a total of 0.64°C over the observation period, equivalent to a rate of 0.24°C per decade. The offshore branch (F4 - F5) warmed more gradually, with a total increase of 0.40°C , or 0.15°C per decade. Combining both branches, the overall WSC warming rate is 0.20°C per decade, amounting to a net increase of 0.54°C from 1997 to 2024.

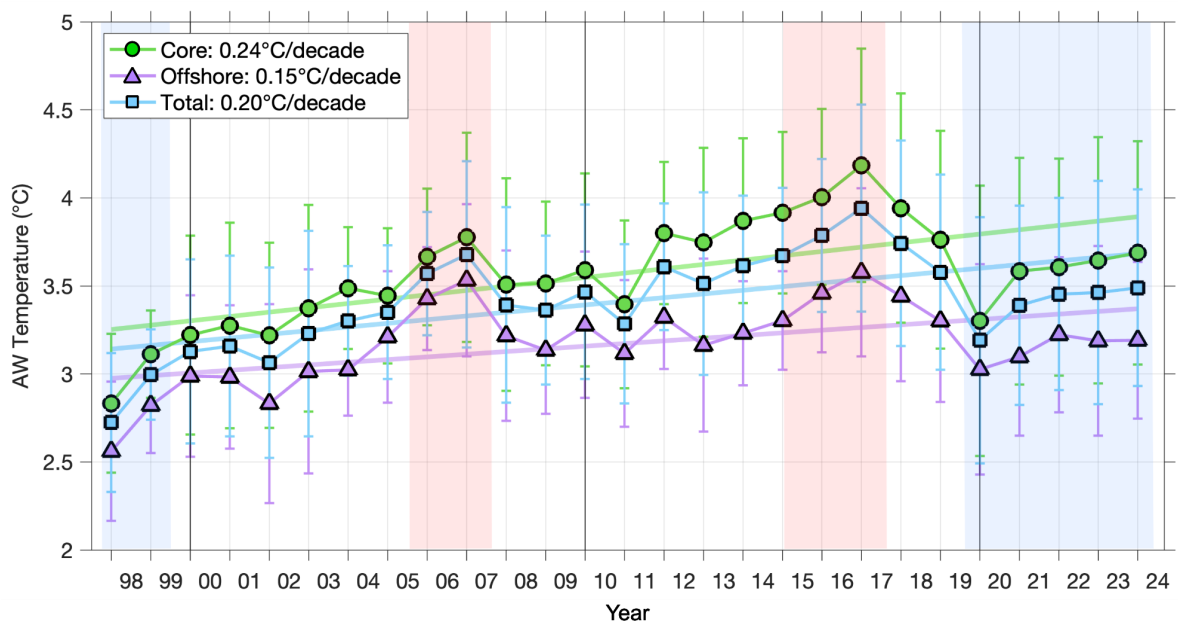


Figure 7. Atlantic Water temperature variability in the WSC branches. Timeseries of annually averaged Atlantic Water (AW) temperatures for the WSC core (F1 - F3), the offshore branch (F4 - F5), and the combined WSC (F1 - F5), with the standard deviation shown as whiskers. Long-term linear trends for each branch are plotted as dotted lines and listed in the legend. Shading marks warm (red) and cold (blue) AW temperature anomalies, as defined in Fig. 5d. Vertical lines indicate the start of each decade.

The warming trend is seasonally consistent. Subsampling for summer-only and winter-only measurements yields comparable trends of 0.19°C per decade and 0.21°C per decade,

respectively (Supplementary Figure 4). On average, AW in the WSC is $\sim 0.4^{\circ}\text{C}$ warmer in summer than in winter. However, during 2005 - 2006 and 2016 - 2017, winter AW temperatures were unusually high and reached levels typically observed in summer, with the 2016 - 2017 winter values exceeding all but three summer measurements. These anomalously warm winters align with the two identified warm AW anomalies (Fig. 5d), suggesting that during such anomalously warm years, winter temperatures are disproportionately elevated, reducing the seasonal amplitude of AW temperature variability.

The comparable trends across seasons indicate that summer hydrographic profiles - typically collected on Arctic expeditions during ice-free periods - can provide a representative measure of longer-term AW inflow temperature trends. However, the strong seasonal cycle (Fig. 2, 5b) and pronounced mesoscale variability in the WSC (von Appen et al., 2016) underscore the limitations of relying on single profiles, which act as snapshots, to resolve interannual variability in such a highly dynamic region.

Although a general warming trend is evident, the increase in AW temperatures is not steady but marked by significant decadal variability. Formal shift detection using a 10-year window identifies three statistically distinct shifts in the AW temperatures over the observational period, defined as multi-year periods with distinct mean AW temperature states (Fig. 8). From 1997 to 2019, AW temperature rose in two steps, with regime shifts in 2004 and 2012. These shifts correspond to the two previously described warm anomalies (Fig. 5d) and resulted in a cumulative warming of approximately 0.7°C , each elevating AW temperatures to new, higher mean states. A third regime shift occurred in 2019, marking the onset of a cooler phase and driven by the prolonged cold anomaly from 2019 to 2024. This shift decreased the mean AW temperature by 0.3°C , effectively reversing much of the warming that occurred since 2012.

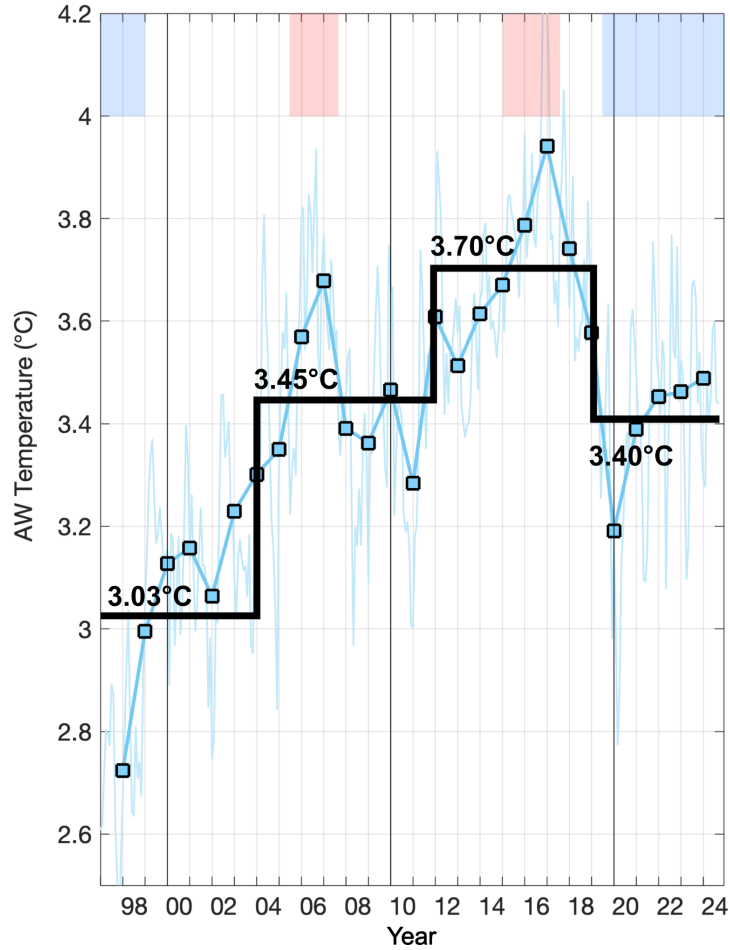


Figure 8. Regime shifts in AW temperature of the WSC. Mean Atlantic Water (AW) temperature across the WSC (as in Fig. 7). Horizontal black lines indicate the mean AW temperatures during three distinct regimes - the mean temperature of which are labelled. Red and blue shading highlight the warm and cold anomalies, respectively, as defined in Fig. 5d.

3.6. Patterns of AW temperature variability

To identify the dominant patterns of AW temperature variability in the WSC, empirical orthogonal function (EOF) analysis was applied to both the original and de-seasoned monthly AW temperature fields. This separation determines if the seasonal cycle and interannual variability are associated with different spatial patterns.

After removing the strong seasonal cycle, the first two EOF modes together account for nearly 80% of the total AW temperature variability (Fig. 9). The third and fourth EOF explain only minor contributions, about 5% and 4% respectively, and are not considered further, along with higher modes (not shown). The first EOF mode alone explains the largest portion of the AW temperature variability (71.5%) and represents a large-scale coherent ‘warm/cold’

pulsing mode, with a spatially uniform temperature structure across the WSC (Fig 9a). The anomalies are strongest in the upper AW layer, with amplitudes up to 2°C near the surface that diminish with depth, approaching 0°C below the AW interface. This structure is consistent with the vertical and horizontal uniformity of the interannual AW temperature anomalies shown in Fig. 5c, and reflects a basin-scale advective signal rather than localised variability.

The corresponding principal component (PC1) captures the temporal evolution of this dominant mode, highlighting the major warm and cold anomaly periods (Fig. 9b). Positive amplitudes coincide with the two warm anomalies, while negative amplitudes correspond to the cold anomalies. The long-term warming trend is also contained within this mode as shown by its persistent positive shift. To assess the influence of the long-term trend, the EOF analysis was repeated with the linear trend removed (not shown). The resulting spatial pattern for the first mode remained similar, with only a modest reduction in explained variance (65.3%), indicating that this dominant mode reflects primarily low-frequency interannual variability, likely driven by advective processes originating upstream, rather than being driven solely by the long-term trend.

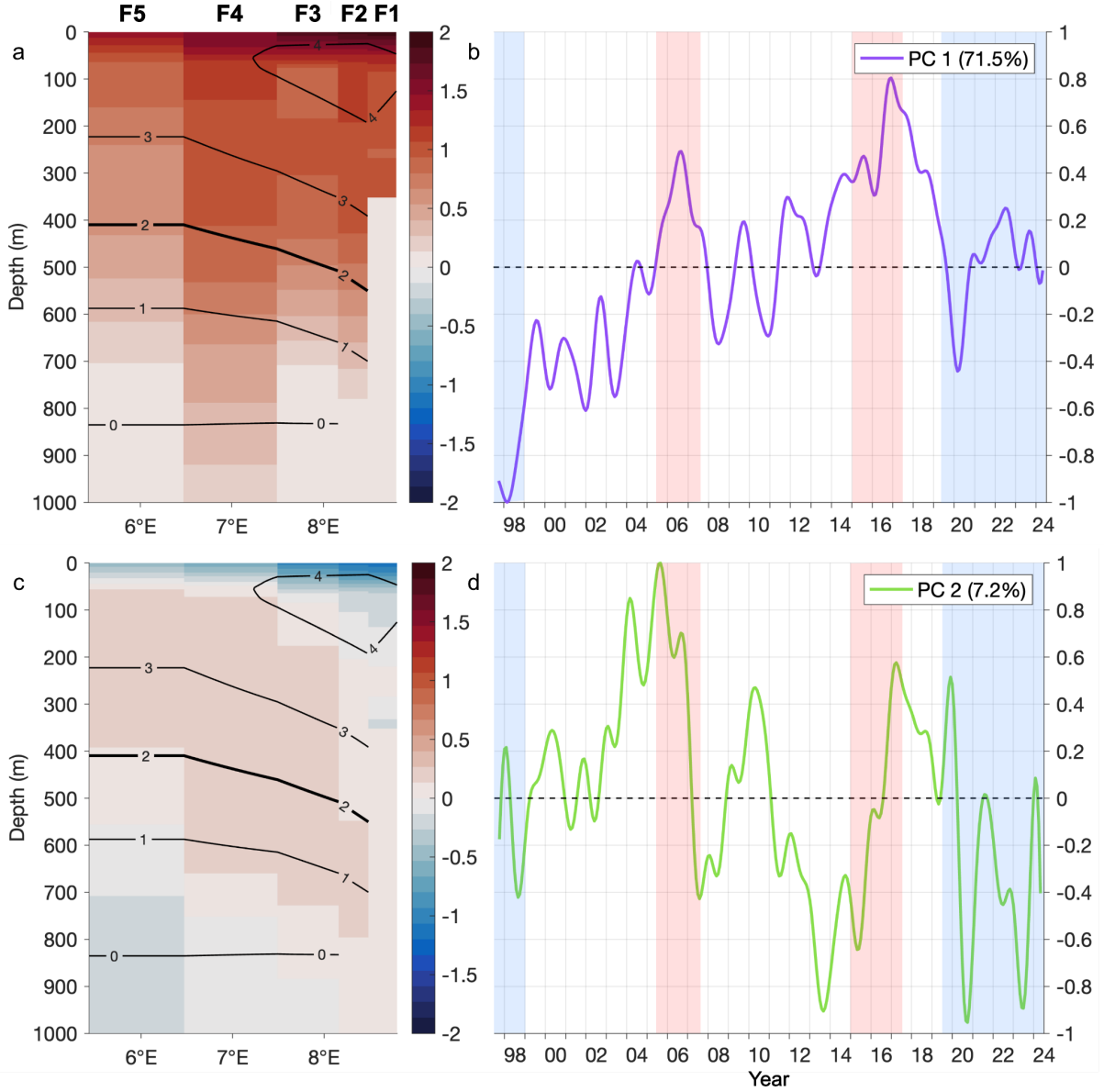


Figure 9. Leading EOFs of AW temperature variability in the WSC. The first two EOFs of the de-seasoned monthly AW temperature across moorings F1 - F5. Maps in (a,c) show the spatial distribution, and (b,d) are the corresponding principal components. The timeseries have been normalised such that the amplitude of the nodes is contained in the maps. Red and blue shading indicate the warm and cold AW anomalies, respectively, as defined in Fig. 5d. Selected mean isotherms are the black contours in the maps; the thick black line represents the mean depth of the AW layer (2°C isotherm).

The second EOF mode accounts for 7.2% of the total variance and reflects vertical changes in the stratification (Fig. 9c). This mode displays a pivoting pattern, with opposite signs in the upper 150m and below, with near-surface cooling and subsurface warming (and vice versa), extending through the AW layer and weakening with depth. Near-surface anomalies reach up to 1°C , while those at the base of the AW layer reach $\sim 0.5^{\circ}\text{C}$. Spatially, this mode also

shows a lateral gradient, with larger variability in the offshore branch and decreasing toward the continental shelf edge.

The associated principal component (PC 2) exhibits more episodic variability than PC 1, suggesting that EOF 2 captures processes that influence stratification on shorter timescales or at smaller spatial scales. During the two warm AW periods, positive PC 2 anomalies (Fig. 9d) indicate near-surface cooling and subsurface warming. This reduced the vertical temperature gradient and weakened the stratification. Conversely, during the two cold AW periods, negative PC 2 anomalies indicate near-surface warming and subsurface cooling, leading to a strengthening of the vertical temperature gradient and increased stratification in the upper water column. This strengthening was particularly pronounced during the second cold anomaly (2019 - 2024). The surface-intensified structure of EOF 2, combined with its episodic nature, indicates that this mode likely reflects transient physical processes. Such processes that can induce shifts in stratification periodically are mesoscale eddies that are prevalent in the WSC (von Appen et al., 2016) or interactions with topography along the continental slope.

Applying EOF analysis to the original (non-deseasoned) monthly AW temperature fields reveals similar spatial patterns, though with the seasonal cycle embedded. The first mode captures 67.4% of the total variability (Supplementary Figure 5b), reflecting the same transect-wide pulsing pattern as EOF1 in the de-seasoned analysis (Fig. 9a). The associated PC1 shows both interannual variability and a clear seasonal cycle, with peaks in September (warm conditions) and minimum values in April (cold conditions) (Fig. 10a). This timing aligns with the seasonal AW temperature maxima and minima (Fig. 10b), confirming that EOF 1 captures the large-scale seasonal warming and cooling of AW superimposed on the interannual signal.

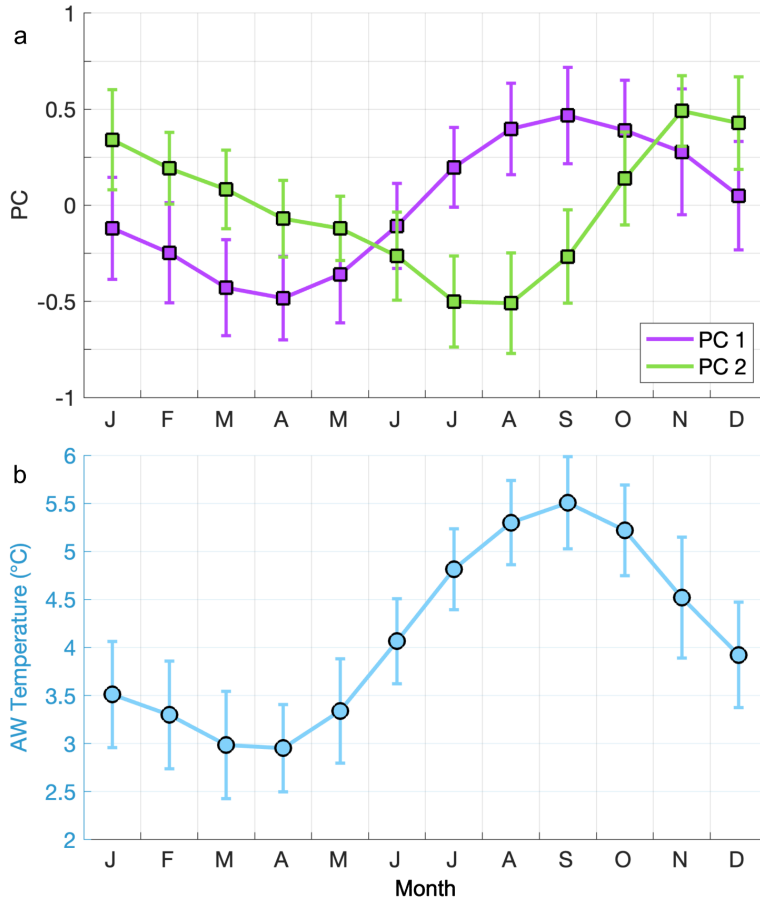


Figure 10. Seasonal cycle of leading AW temperature modes. (a) Mean seasonal cycle of PC 1 and PC 2 from the AW temperature EOF analysis (see Supplementary Figure 5c and 5e respectively). (b) Mean seasonal cycle of AW temperature at 75 m depth across the WSC. Error bars indicate ± 1 standard deviation.

The second EOF mode of the original data (Supplementary Figure 5d) similarly captures vertical shifts in stratification, as seen in the de-seasoned results (Fig. 9c). The associated PC 2 (Supplementary Figure 5e) exhibits a clear seasonal cycle, with maximum values peaking in November and minimum values in July-August (Fig. 10a). This seasonal structure reflects the warmer near-surface waters in summer while the temperatures cool below 200m, which increases stratification in the AW layer, followed by weaker stratification in winter as surface temperatures cool.

A seasonal progress of PC 1 and PC 2 shows a strong correlation ($R = 0.7$) with a 3-month lag (Fig. 10a), suggesting that changes in vertical stratification (PC 2) have a lagged response to the summer-intensified surface-driven AW warming (PC 1). This lag is likely associated with the downward propagation of the seasonal thermocline, which modifies

stratification throughout the AW layer, that can be observed in both the core and offshore branch of the WSC (Fig. 4c,d).

4. Discussion

4.1. Long-term AW warming trends

One of the key findings from the 27-year observation record was the robust, statistically significant ($P < 0.05$) warming trend in AW temperatures across the WSC, despite pronounced interannual and decadal variability. Warming was strongest in the WSC core, at a rate of 0.24°C per decade, and slower in the offshore branch at 0.15°C per decade (Fig. 7). These different rates reflect the distinct pathways of the two branches originating from the Norwegian Atlantic Current (Fig 1). The offshore branch, which has longer advection timescales (Mauritzen et al., 2011), undergoes greater cumulative cooling, primarily through air-sea heat loss along the NwAFC, whereas temperature changes along the NwASC are largely governed by lateral oceanic heat transport (Huang et al., 2023). These differing mechanisms of heat loss help explain the differing long-term AW warming rates along the two WSC branches. The resulting increased lateral density gradient may also contribute to enhanced baroclinic instability.

The warming rates observed here differ markedly from the findings of Beszczynska-Möller et al. (2012), who estimated a rate of 0.61°C per decade using the observations from 1997 to 2010. If extrapolated, that would be equivalent to a total warming of 1.6°C over the 27 years examined here - nearly three times the actual total observed warming of 0.54°C . This discrepancy arises from the influence of short-term variability on trends derived from limited time periods, as demonstrated by the formal shifts in the AW temperature (Fig. 8). Notably, the initial 10 years of AW temperatures were flanked by a cold anomaly at the start of the record which transitioned to a warm anomaly in 2005 - 2006, driving a rapid 0.8°C increase in AW temperature and shifting the system into a warmer regime (Fig. 7, 8). When viewed over the full 27-year record, formal regime shift analysis reveals a further stepwise increase in AW temperature in 2012 and marking the peak of the warming period, followed by a multi-year cooling period beginning in 2019 and during which AW temperatures declined by 0.27°C . The second cold anomaly fell within this shift, returning to values similar to those before 2012. While AW temperatures remained above pre-2000 levels, this recent cooling and the discrepancy in the warming rates between those presented here over 27 years and the 13-year estimates from Beszczynska-Möller et al., (2012) highlights the nonlinear and

episodic nature of long-term change. It also underscores the risk of over-interpreting trends from relatively short timescales because they may represent shorter-term variability rather than a real long-term trend. Although 13 years constitutes a relatively long observational record, it highlights the persistent challenge of capturing sustained climate signals in-situ.

Despite this variability, the underlying long-term warming trend is consistent with both model simulations and other broader regional observations. For example, Muijlwijk et al., (2018) reported a warming of 0.33°C per decade from 1980 to 2012 using a forced global ocean model. Observational studies also reported warming in the deeper waters (~ 2500 m) of the WSC and in the Greenland Sea Deep Water, albeit at smaller amplitudes - approximately 0.1°C per decade between 1997 - 2014 (von Appen et al., 2015) and 0.04°C per decade from 2010 - 2022 (Karam et al., 2024). The reported reduced warming of the deeper water from 2010 aligns with the broader pattern of slowdown of AW temperature increases after 2012 (Fig. 7).

Interestingly, the long-term WSC AW warming trend contrasts with conditions upstream. At Svinøy (62°N) in the Norwegian Atlantic Slope Current (NwASC), north of the Faroe Islands, no net AW warming was recorded over 1995 - 2020 (Orvik, 2022). This is principally attributed to a rapid cooling of almost 1°C from 2015 - 2020 that effectively offset the earlier, more gradual warming. Taking the timeseries from 1995 - 2015, AW at Svinøy warmed by approximately 0.8°C , consistent with the 0.7°C warming observed in the WSC between 1998 and 2018, considering the expected advection time lag of 2 - 3 years (Holliday et al., 2008). The subsequent cooling at Svinøy propagated northward, reaching Fram Strait around 2017, and coincided with the regime shift to cooler AW temperatures in the WSC in 2019 (Fig. 7, 8). However, while Svinøy temperatures returned to pre-2000 levels, AW temperatures in the WSC remained elevated. This divergence reflects the influence of regional damping mechanisms in the Nordic Seas that buffer or modulate upstream anomalies. Rising atmospheric temperatures over the Nordic Seas in recent decades (Isaksen et al., 2022) have weakened the ocean-atmosphere temperature gradient and reduced the air-sea flux that weakens surface cooling and controls much of the AW temperature change along the AW inflow to Fram Strait (Huang et al., 2023). At the same time, enhanced stratification from Arctic freshwater input and local atmospheric forcing can also insulate the AW layer (von Appen et al., 2021; Wang et al., 2023), further decoupling the WSC temperature evolution from upstream variability. These processes can modulate both the amplitude and persistence of temperature anomalies, allowing warm AW signals to persist or even be locally amplified in Fram Strait, even when upstream sources cool.

4.2. Extended Timescales of AW Warming

By incorporating historical datasets, the observational record of AW temperature in the WSC can be extended to 56 years (1969 - 2024), offering a broader context for the observed longer-term change. Combining CTD data from 1969 - 1997 with the more recent WSC moorings records from 1997 - 2024 yields a statistically significant warming rate of 0.36°C per decade ($P < 0.05$; Fig. 11). When using mooring data alone - including earlier deployments from 1971 - 1997 - the rate decreases slightly to 0.27°C per decade, yet remains notably faster than the 0.20°C per decade trend observed in the most recent 27-year record.

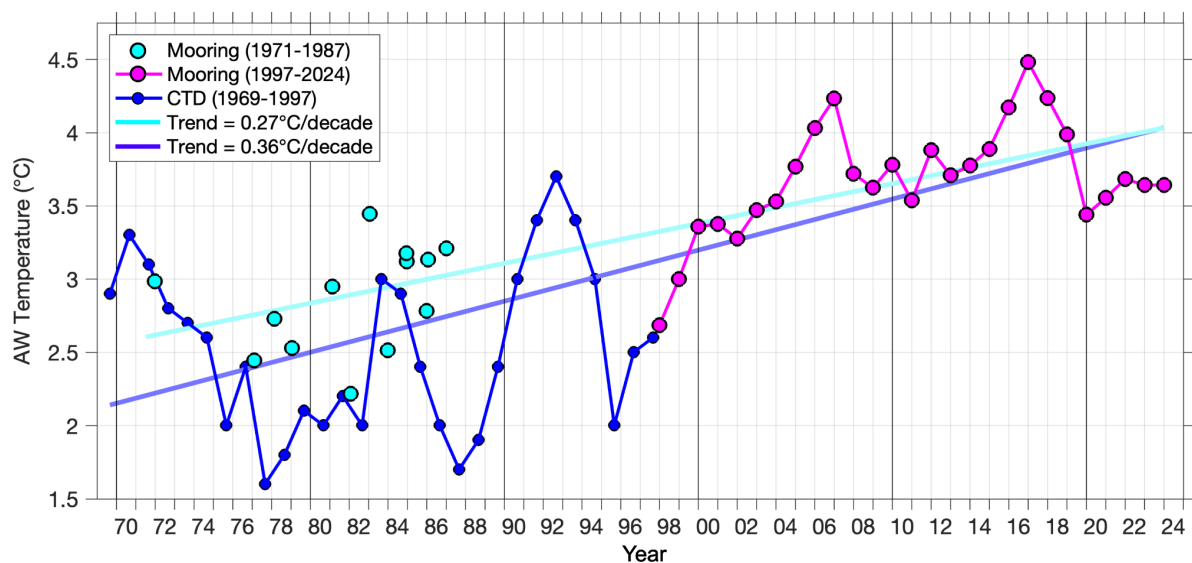


Figure 11. Historical AW temperature record in the WSC. Annual mean AW temperatures in the WSC derived from both historical and the present mooring-based observations. Pre-1997 mooring data (cyan) represents temperatures between 100 - 300 m depth within 50km of moorings F3 and F4. Post-1997 data (from AWI; pink) show temperatures averaged between 100 - 300 m at F3 and F4. Historical CTD data (dark blue) are 100 - 300 m averages from 1969 - 1997. Linear trend lines for each dataset are shown; the decadal warming rates are included in the legend.

The differences between datasets are partly due to their methodological characteristics. The CTD dataset represents instantaneous ‘snapshots’ of the dynamic system, capturing higher-frequency variability driven by mesoscale and seasonal processes. This results in the greater temperature variability in the CTD record (1969 - 1997), especially compared to the earlier mooring records (1971 - 1987) which are averaged over longer timescales, suppressing some of the high-frequency variability and providing a more stable estimate of

long-term trends. As a result, while the seasonal AW warming rate is comparable year-round (Supplementary Figure 4), the summer-based CTD profiles may overemphasize seasonal and high-frequency variability relative to the year-round signal.

Despite these methodological differences, extending the observational period using both datasets supports the conclusion that AW temperatures in the WSC have undergone persistent long-term warming over the last five decades. This sustained trend persists through interannual and decadal variability and is consistent with the wider regional warming observed across the Nordic Seas and North Atlantic since the 1970s (Polyakov et al., 2023; Saes et al., 2022). These findings reinforce that the multi-decade persistence of this AW warming in Fram Strait is a sustained regional signal of ongoing climate change, rather than a short-term anomaly.

4.3. Advection of AW temperature signals through Fram Strait

4.3.1. Upstream origins of AW temperature variability

AW temperatures in the WSC are marked by distinct multi-annual warm and cold anomalies, rather than changing at a constant rate. Over the 27-year record, two warm (2005 - 2007 and 2016 - 2018) and two cold (1997 - 1999 and 2019 - 2024) anomalies were identified (Fig. 5d), each persisting for 2–4 years and spanning the full width of the WSC with minimal lateral gradients (Fig. 5c). This spatial uniformity is consistent with the dominant mode of variability of AW temperature captured by EOF 1 (Fig. 9a), which represents a coherent, large-scale ‘pulsing’ pattern and indicates large-scale advective processes rather than localized variability as the primary driver.

The timing and structure of these anomalies align closely with upstream temperature variability in the Norwegian Atlantic Slope Current (NwASC). Previous studies have demonstrated the northward propagation of AW temperature signals from the North Atlantic through the Nordic Seas and into Fram Strait (Holliday et al., 2008; Karcher et al., 2003; Chafik et al., 2015; Muilwijk et al., 2018; Polyakov et al., 2023). For example, two warm AW anomalies observed at Svinøy (2002 - 2005 and 2014 - 2016) precede the warm anomalies in the WSC (2005 - 2007 and 2016 - 2018), while earlier cold anomalies at Svinøy (1995 - 1998 and 2013 - 2015) precede the WSC cold anomalies (1997 - 1999 and 2019 - 2024) (Orvik, 2022). These lags are consistent with the estimated propagation speeds for hydrographic anomalies ($\sim 2 \text{ cm s}^{-1}$) along the boundary current system (Årthun and Eldevik, 2016; Broomé and Nilsson, 2018) which are approximately one order of magnitude slower

than the mean current velocity of the NwASC but reflect the net effect of advection and diffusion. These temporal alignments reinforce that low-frequency AW temperature variability in Fram Strait is set by upstream anomalies originating in the North Atlantic that propagate northwards along the AW pathway.

4.3.2. Downstream advection of AW temperature variability

The WSC anomalies also propagate downstream into the Arctic Ocean. Long-term observations north of Svalbard have measured the downstream AW inflow, i.e., the Svalbard Branch, since 2012 (Renner et al., 2018) and provide additional evidence of coherent advective transport. A comparison of the monthly AW temperature anomalies between 2012 - 2022 in the WSC and along the shelf break of the Svalbard Branch show that AW temperature anomalies in the Svalbard Branch lag those in the WSC core by approximately 2 months (Fig. 12). This lag is consistent with flow speeds of $0.14 - 0.18 \text{ ms}^{-1}$ in the WSC (Table 1) and 0.12 ms^{-1} in the Svalbard Branch (Renner et al., 2018). A strong correlation between the two ($R = 0.7$, $P < 0.05$) supports the findings of Pérez-Hernández et al., (2019) and indicates that AW anomalies propagate coherently downstream along the AW pathway.

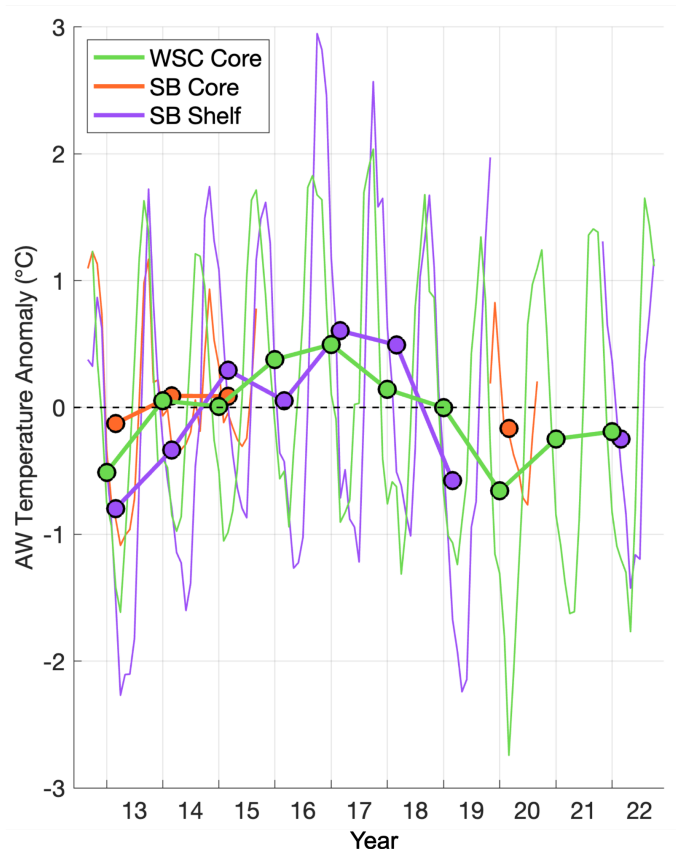


Figure 12. Downstream advection of AW temperature anomalies. Comparison of monthly (thin lines) and annual (circles) AW temperature anomalies in the WSC core (green), the

Svalbard Branch (SB) core (orange), and SB shelf (purple). Mooring locations are marked in Fig. 1. Annual means in the Svalbard Branch are calculated with a 2-month lag relative to the WSC to reflect the downstream advection of anomalies.

Despite this coherence, the temperature anomalies weaken downstream. On average, the Svalbard Branch is over 2.5°C colder than the WSC core (Fig. 12), suggesting significant heat loss en route—likely due to air–sea fluxes and lateral mixing. Interannual variability also differs subtly: while both branches warmed from 2012 to 2017 and then cooled, the Svalbard Branch returned to warmer anomalies by 2020, while the WSC core continued cooling. This divergence suggests that although advection likely governs the large-scale temperature structure and longer-term anomalies, local processes—such as seasonal variability, mixing, and ice-ocean interactions—can modulate or amplify the higher frequency variability on shorter timescales or more regionally (Renner et al., 2018; Lundsgaard et al., 2021).

The signal continues into the Arctic Ocean interior. The seasonally varying hydrographic properties are advected into the Nansen Basin and remain detectable in the transformed AW found along the boundary current off Severnaja Zemlya (Ruiz-Castillo et al., 2023). For example, a warm AW anomaly observed in Fram Strait in 1999 reached the Eurasian Basin by 2004 (Polyakov et al., 2005) and the Canadian Basin by 2010 (Polyakov et al., 2023). These observations indicate that the AW temperature variability in the WSC largely sets the initial conditions for AW inflow to the central Arctic Ocean, and demonstrates that a continued, unambiguous long-term warming is anticipated. While AW also enters the Arctic Ocean through the Barents Sea Opening (BSO), much of that heat is lost to the atmosphere before reaching the central Arctic (Schauer et al., 2008; Smedsrød et al., 2022), thus the AW inflow through Fram Strait via the WSC remains the dominant oceanic heat source to the Arctic Ocean interior. If a similar propagation continues, the second warm anomaly (2017 - 2019) is expected to follow, with ORAS5 reanalysis showing its signature appearing in the Eurasian Basin around 2022 (Supplementary Figure 6), consistent with a 5 - 6 year lag, and would be anticipated in the Canadian Basin around ~ 2029. These observations confirm the continued downstream transport of AW anomalies into the Arctic Ocean interior, in line with earlier findings (Körtke et al., 2024; Polyakov et al., 2023, 2005).

4.3.3. Other drivers of AW temperature variability

The strong correlation and consistent lag between upstream and downstream AW temperature anomalies underscores the dominant role of oceanic advection in transmitting

anomalies along the full AW pathway into the Arctic, yet additional local and regional processes can also modulate these signals. Temperature anomalies often extended further west across central Fram Strait beyond the WSC and its recirculation branches, reaching 4°W and the Greenland continental shelf (Supplementary Figure 3), suggesting a more regional driver. Moreover, the long-term AW warming trend observed in the WSC is not mirrored at the upstream Svinøy section (Orvik, 2022), suggesting that local thermodynamic forcing, such as air-sea heat exchange, may also contribute to temperature variability over longer timescales.

Atmospheric forcing can further modulate interannual AW temperature variability in both the Nordic Seas and Fram Strait, impacting the strength of the AW circulation (Chatterjee et al., 2018; Heukamp et al., 2023; McPherson et al., 2023; Muilwijk et al., 2018). Specifically, McPherson et al., (2024) linked several of the multi-annual cold anomalies observed in the WSC (Fig. 7) to persistent atmospheric blocking. The blocking is characterised by a high pressure anomaly over northern Europe which was associated with a low sea-level pressure anomaly over the Arctic. These conditions strengthened the cold air export through Fram Strait, increasing ocean heat loss to the atmosphere and subsequent AW cooling. In addition, the associated winds promoted an offshore Ekman transport which drove an anomalous geostrophic flow opposing the mean NwASC direction, slowing the NwASC and WSC, and further intensifying the AW cooling. The cold regime shift in 2019 demonstrated how the influence of advection and atmospheric blocking can be seen as complementary: large-scale upstream anomalies set the broader temperature state, while atmospheric conditions - especially when sustained - can further modulate or even enhance these signals locally and contribute to regime transitions. While we do not explicitly diagnose blocking events here, this interpretation supports the idea that large-scale atmospheric forcing modulating AW inflow into Fram Strait and interacts with the advection of upstream anomalies (e.g., McPherson et al., 2024; Holliday et al., 2008).

While atmospheric blocking primarily affects temperature via changes in AW inflow, it can also affect salinity. The longer residence time associated with slowed-down currents and subsequent surface heat flux potentially freshens the surface layers, while blocking-induced wind patterns may also affect upper-ocean salinity through altered sea ice export and wind-driven mixing (Holliday et al., 2020; Ionita et al., 2016). Over longer timescales, salinity variability tends to be more strongly influenced by upstream advection of hydrographic anomalies and the influence of large-scale atmospheric forcing (Hátún et al., 2005; Holliday et al., 2020; Park et al., 2022; Polyakov et al., 2023). These mechanisms may partially account for the observed co-occurrence of warm/saline and cold/fresh anomalies in the WSC

(Fig. 6c,d). The significant correlation between the temperature and salinity anomalies ($R = 0.88$) reflects this co-variability, often resembling partial density compensation, where temperature and salinity anomalies counteract each other's effect on density. In the WSC, the temperature anomalies have a slightly stronger influence on density and do not fully compensate for the salinity anomalies $((\alpha \times SD(\theta)) / (\beta \times SD(S_A)) = 1.2$), where α and β are the thermal and saline expansion coefficients, and SD is the standard deviation of temperature (θ) and salinity (S_A) respectively. However, given that temperature and salinity nearly compensate, the expected influence on changes in geostrophic velocity - and thus transport anomalies - is reduced compared to what would be inferred from temperature anomalies alone.

Changes in the AW properties influence the broader density-driven circulation. Due to its relatively high salinity, the dense AW in the WSC subducts beneath the fresher PW that flows southwards in the EGC (Hofmann et al., 2024), forming the deep warm core in the EGC that contributes to the Denmark Strait overflow and, ultimately, North Atlantic Deep Water (Håvik et al., 2017). The persistent AW warming observed in Fram Strait also reduces AW density and could weaken the lateral density gradient that drives the recirculation and subduction intensity. Given that temperature anomalies have a slightly stronger influence on density than salinity, this warming is likely to play a measurable role in modulating these dynamics. However, since temperature and salinity tend to partially compensate and salinity still contributes substantially to the density structure, the overall impact will depend on their combined variability, particularly on interannual timescales. Meanwhile, basin-scale warming in the Lofoten and Norwegian Basins in the Nordic Seas has resulted in recent density loss, primarily driven by temperature increases rather than salinity decline (Shi et al., 2024; Wang et al., 2023). This broader warming has already contributed to reduced overflow density and storage volume within the Nordic Seas, posing a more direct constraint on NADW formation than the local changes observed in Fram Strait.

4.4. Further impacts of AW temperature variability in the WSC

The long-term and interannual variability of AW temperatures in the WSC have significant and far-reaching implications for the marine ecosystem, cryosphere and sea ice (Soltwedel et al., 2016, Salter et al., 2023; Ahme et al., 2023). Variations in AW temperatures directly influence vertical stratification, which in turn influences nutrient fluxes into the surface layer. Reduced vertical mixing during warm periods can limit the upward transport and availability

of nutrients - processes that are critical for sustaining primary productivity and regulating broader food web dynamics (von Appen et al., 2021).

One clear example of ecosystem response occurred following the warm AW anomaly between 2005 and 2007 (Fig. 5d), which preceded a major shift in phytoplankton composition (Nöthig et al., 2015). Soltwedel et al., (2016) linked this warm period to increased growth of sub-Arctic primary producers, as well as changes in the abundance and reproductive output of sub-Arctic species. These biological shifts triggered cascading effects throughout the open-ocean ecosystem, impacting organisms from the pelagic zone to the deep seafloor. Conversely, Jackowski et al. (2025) documented a substantial decline in cell abundance within the WSC core during July 2021 relative to 2014, attributing the decrease to the anomalously cold AW conditions. Together, these biological responses illustrate how AW temperature variability can directly shape microbial communities and, by extension, influence broader ecosystem structure and function.

AW temperature variability also has important cryospheric impacts. In Svalbard, warmer AW in the WSC has been linked to glacier mass loss, with ocean-driven warming contributing to higher ablation rates and dominating the accelerated glacier retreat (Foss et al., 2024). Farther west, the interannual temperature variability in the WSC is advected westwards and partly controls the warm water inflow to the marine-terminating glaciers on the Northeast Greenland continental shelf. This recirculation is modulated by anomalous atmospheric conditions over Svalbard (Heukamp et al., 2023; McPherson et al., 2023). Below the 79 North Glacier in Northeast Greenland, the AW warming has been shown to drive enhanced basal melt rates, with implications for glacier stability (McPherson et al., 2024; Wekerle et al., 2024), reinforcing the critical role of AW as a driver of both local and basin-scale changes in glacier dynamics.

The interaction between AW temperatures and sea ice further amplifies the broader climatic and ecological response. Warmer AW increases oceanic heat flux, contributing to enhanced sea ice melt as the AW cools to near-freezing temperatures (Rudels, 2010). Positive AW temperature anomalies have been associated with reduced sea ice concentration, while cold anomalies tend to correspond to increased sea ice cover (Fig. 5a,d). A similar pattern was also observed on the eastern flank of the EGC, where an episodic intrusion of positive AW temperature anomalies resulted in local sea ice thinning and retreat, with downstream effects on the broader sea ice cover (de Steur et al., 2023).

5. Conclusions

This study presents new insights and a comprehensive assessment of long-term trends and variability in the West Spitsbergen Current (WSC) using a 27-year record (1997 - 2024) from the mooring array in eastern Fram Strait (4–9°E). It extends the analysis of Beszczynska-Möller et al., (2012), which used the same mooring array but spanned from 1997–2010, presenting a multi-decadal perspective on Atlantic Water (AW) temperature variability at the Fram Strait gateway to the Arctic Ocean.

There is a clear and unequivocal multi-decadal warming trend in the AW, with temperatures increasing at a rate of 0.20°C per decade - amounting to a total warming of 0.54°C over the 27-year mooring record. This rate is slower than the earlier 1997 - 2010 estimate, due to the influence of pronounced interannual variability and differences in record lengths. When combined with historical hydrographic data extending back to 1969, the warming trend reflects robust, multi-decadal AW warming over the past 56 years. The warming is observed year-round, with similar trends in both summer and winter that confirm summer-based CTD profiles reliably represent annual AW temperature conditions, with a typical warm-season offset of ~0.6°C relative to the annual mean.

Distinct multi-annual warm and cold anomalies were observed across both branches of the WSC and throughout the AW layer. Two prominent warm periods occurred in 2005 - 2007 and 2016 - 2018, and two cold periods between 1997 - 1999 and 2019 - 2024. These temperature anomalies often co-occurred with salinity anomalies, with warm periods generally linked to more saline conditions and cold periods to fresher waters. These hydrographic anomalies also left clear imprints on the Arctic marine ecosystem, propagating through the entire food web (e.g., Soltwedel et al., 2016; Jackowski et al. 2025; Dannheim et al., 2025), and have influenced cryospheric processes, including glacier retreat in Svalbard and basal melt beneath marine-terminating glaciers in Northeast Greenland.

The observed interannual variability in AW temperatures is driven by both the upstream advection of signals from the Nordic Seas and local atmospheric forcing. Temperature anomalies propagate northward into the Arctic Ocean along the AW inflow pathway of the Svalbard Branch, typically with a 2-month lag relative to Fram Strait, and arriving in the Eurasian Basin after a further ~6 years. This underscores the role of Fram Strait as a key gateway for upstream AW signal transport into the Arctic. The persistent long-term warming, evident in both the in-situ records presented here and predicted by CMIP climate simulation

projections (He et al., 2024; Shu et al., 2022) suggests that the temperature of the AW flowing northward through Fram Strait will continue to rise; the resultant increase in oceanic heat transport will have significant and far-reaching implications for the future state of the Arctic Ocean.

Acknowledgements

This work is funded by the European Union as part of the EPOC project (Explaining and Predicting the Ocean Conveyor). Views and opinions expressed are however those of the author(s) only and do not necessarily reflect those of the European Union. Neither the European Union nor the granting authority can be held responsible for them.

The maintenance of the mooring array in the WSC used in this study was supported by multiple different institutional, national, and European projects: Helmholtz Infrastructure Initiative FRAM (FRontiers in Arctic marine Monitoring), Cooperative Project RACE, 0F0651D of the German Federal Ministry of Education and Research, the EU project ASOF–N (Arctic–Subarctic Ocean Flux Array for European Climate –North; contract number EVK2-CT-200200139), the EU Integrated Project DAMOCLES (Developing Arctic Modelling and Observing Capabilities for Long-term Environment Studies, contract number 018509GOCE), and the EU Collaborative Project ACOBAR (Grant Agreement no. 212887). The A-TWAIN moorings are funded through the Fram Centre flagship “Sea ice in the Arctic Ocean, technology and agreements, project number 66050, and the Research Council of Norway project SIOSInfraNor (no. 269927).

We thank the captains, crews, and scientific parties on the R/V Polarstern and the R/V Maria S. Merian during the multiple expeditions. Thanks also to all who processed the West Spitsbergen Current mooring data over the years. The following cruises (listed with grant numbers) contributed to the maintenance of the mooring array: R/V Polarstern: ARK-XIII/3, ARK-XIV/2, ARK- XIX/3c, ARK-XIX/4b, ARK-XV/3, ARK-XVI/1, ARK-XVI/2, ARK-XVII/1, ARK-XVIII/1, ARK-XX/1, ARK-XX/2, ARK-XXI/1b, ARK-XXII/1c, ARK-XXIII/2, ARKXXIV/1, ARK-XXIV/2, ARK-XXV/2, ARK-XXVI/1, ARK-XXVI/2, ARK-XXVII/1, ARK-XXVII/2, PS85 (AWI_PS85_03), PS93.1 (AWI_PS93.1_02), PS99 (AWI_PS99_00), PS100 (AWI_PS100_01), PS107 (AWI_PS107_04), PS114 (AWI_PS114_01), PS121 (AWI_PS121_06), PS126 (AWI_PS126_07), PS131 (AWI_PS131_04), PS136 (AWI_PS136_04), PS143.2 (AWI_PS143.2_00); R/V Maria S. Merian: MSM02, MSM29, MSM76 (GPF 18-1_1), MSM93 (GPF 18-1_33); R/V Heincke: HE451-2; and R/V Lance.

Data Availability

The gridded data of temperature and salinity from each mooring (F1 - F7) in the West Spitsbergen Current used for this analysis is available at (*waiting for DOI*). The measured mooring data (F1 - F7) from 1997 - 2016 is available at (von Appen et al., 2019) <https://doi.pangaea.de/10.1594/PANGAEA.900883>; from 2016 to 2018 at (von Appen, 2019) <https://doi.pangaea.de/10.1594/PANGAEA.904565>; and from 2018 to 2024 at (Hoppmann, 2024) <https://doi.pangaea.de/10.1594/PANGAEA.959812>. The historical WSC temperature data from the moorings (1971 - 1987) was provided in Jónsson and Foldvik (1992), and CTD data (1969 - 1997) from Saloranta and Haugan, (2001) (and in Supplementary Table 4). The A-TWAIN mooring data is available from 2012 - 2013 at <https://doi.org/10.21334/npolar.2017.5f53146f>, from 2013 - 2015 at <https://doi.org/10.21334/npolar.2020.c972dd9c>; from 2015 - 2017 at <https://doi.org/10.21334/npolar.2020.ceb74f92>; from 2017 - 2019 at <https://doi.org/10.21334/npolar.2020.e7041026>, from 2019 - 2020 at <https://doi.org/10.21334/npolar.2022.d3a5adc2>; and from 2021 - 2022 at <https://doi.org/10.21334/npolar.2024.86ec6869>.

References

- Aagaard, K., Carmack, E.C., 1989. The role of sea ice and other fresh water in the Arctic circulation. *J. Geophys. Res. Oceans* 94, 14485–14498.
<https://doi.org/10.1029/JC094iC10p14485>
- Aagaard, K., Foldvik, A., Hillman, S.R., 1987. The West Spitsbergen Current: Disposition and water mass transformation. *J. Geophys. Res.* 92, 3778.
<https://doi.org/10.1029/JC092iC04p03778>
- Årthun, M., Eldevik, T., 2016. On Anomalous Ocean Heat Transport toward the Arctic and Associated Climate Predictability. *J. Clim.* 29, 689–704.
<https://doi.org/10.1175/JCLI-D-15-0448.1>
- Banks, H.T., Wood, R.A., Gregory, J.M., Johns, T.C., Jones, G.S., 2000. Are observed decadal changes in intermediate water masses a signature of anthropogenic climate change? *Geophys. Res. Lett.* 27, 2961–2964. <https://doi.org/10.1029/2000GL011601>
- Barnett, T.P., Pierce, D.W., AchutaRao, K.M., Gleckler, P.J., Santer, B.D., Gregory, J.M., Washington, W.M., 2005. Penetration of Human-Induced Warming into the World's Oceans. *Science* 309, 284–287. <https://doi.org/10.1126/science.1112418>
- Beszczynska-Möller, A., Fahrbach, E., Schauer, U., Hansen, E., 2012. Variability in Atlantic water temperature and transport at the entrance to the Arctic Ocean, 1997–2010. *ICES J. Mar. Sci.* 69, 852–863. <https://doi.org/10.1093/icesjms/fss056>
- Boyd, T.J., D'Asaro, E.A., 1994. Cooling of the West Spitsbergen Current: Wintertime Observations West of Svalbard. *J. Geophys. Res.* 99, 22597.
<https://doi.org/10.1029/94JC01824>

- Broomé, S., Nilsson, J., 2018. Shear dispersion and delayed propagation of temperature anomalies along the Norwegian Atlantic Slope Current. *Tellus Dyn. Meteorol. Oceanogr.* 70, 1453215. <https://doi.org/10.1080/16000870.2018.1453215>
- Chatterjee, S., Raj, R.P., Bertino, L., Skagseth, Ø., Ravichandran, M., Johannessen, O.M., 2018. Role of Greenland Sea Gyre Circulation on Atlantic Water Temperature Variability in the Fram Strait. *Geophys. Res. Lett.* 45, 8399–8406. <https://doi.org/10.1029/2018GL079174>
- de Steur, L., Hansen, E., Mauritzen, C., Beszczynska-Möller, A., Fahrbach, E., 2014. Impact of recirculation on the East Greenland Current in Fram Strait: Results from moored current meter measurements between 1997 and 2009. *Deep Sea Res. Part Oceanogr. Res. Pap.* 92, 26–40. <https://doi.org/10.1016/j.dsr.2014.05.018>
- de Steur, L., Sumata, H., Divine, D.V., Granskog, M.A., Pavlova, O., 2023. Upper ocean warming and sea ice reduction in the East Greenland Current from 2003 to 2019. *Commun. Earth Environ.* 4, 261. <https://doi.org/10.1038/s43247-023-00913-3>
- Docquier, D., Koenigk, T., Fuentes-Franco, R., Karami, M.P., Ruprich-Robert, Y., 2021. Impact of ocean heat transport on the Arctic sea-ice decline: a model study with EC-Earth3. *Clim. Dyn.* 56, 1407–1432. <https://doi.org/10.1007/s00382-020-05540-8>
- E.U. Copernicus Marine Service Information (CMEMS), n.d. Global Ocean Gridded L 4 Sea Surface Heights And Derived Variables Reprocessed 1993 Ongoing. <https://doi.org/10.48670/moi-00148>
- Foss, Ø., Maton, J., Moholdt, G., Schmidt, L.S., Sutherland, D.A., Fer, I., Nilsen, F., Kohler, J., Sundfjord, A., 2024. Ocean warming drives immediate mass loss from calving glaciers in the high Arctic. *Nat. Commun.* 15, 10460. <https://doi.org/10.1038/s41467-024-54825-7>
- Hattermann, T., Isachsen, P.E., Appen, W., Albretsen, J., Sundfjord, A., 2016. Eddy-driven recirculation of Atlantic Water in Fram Strait. *Geophys. Res. Lett.* 43, 3406–3414. <https://doi.org/10.1002/2016GL068323>
- Hátún, H., Sandø, A.B., Drange, H., Hansen, B., Valdimarsson, H., 2005. Influence of the Atlantic Subpolar Gyre on the Thermohaline Circulation. *Science* 309, 1841–1844. <https://doi.org/10.1126/science.1114777>
- Håvik, L., Pickart, R.S., Våge, K., Torres, D., Thurnherr, A.M., Beszczynska-Möller, A., Walczowski, W., von Appen, W.-J., 2017. Evolution of the East Greenland Current from Fram Strait to Denmark Strait: Synoptic measurements from summer 2012. *J. Geophys. Res. Oceans* 122, 1974–1994. <https://doi.org/10.1002/2016JC012228>
- He, Y., Shu, Q., Wang, Q., Song, Z., Zhang, M., Wang, S., Zhang, L., Bi, H., Pan, R., Qiao, F., 2024. Arctic Amplification of marine heatwaves under global warming. *Nat. Commun.* 15, 8265. <https://doi.org/10.1038/s41467-024-52760-1>
- Hersbach, H., Bell, B., Berrisford, P., Hirahara, S., Horányi, A., Muñoz-Sabater, J., Nicolas, J., Peubey, C., Radu, R., Schepers, D., Simmons, A., Soci, C., Abdalla, S., Abellan, X., Balsamo, G., Bechtold, P., Biavati, G., Bidlot, J., Bonavita, M., De Chiara, G., Dahlgren, P., Dee, D., Diamantakis, M., Dragani, R., Flemming, J., Forbes, R., Fuentes, M., Geer, A., Haimberger, L., Healy, S., Hogan, R.J., Hólm, E., Janisková, M., Keeley, S., Laloyaux, P., Lopez, P., Lupu, C., Radnoti, G., De Rosnay, P., Rozum, I., Vamborg, F., Villaume, S., Thépaut, J., 2020. The ERA5 global reanalysis. *Q. J. R. Meteorol. Soc.* 146, 1999–2049. <https://doi.org/10.1002/qj.3803>
- Heukamp, F.O., Aue, L., Wang, Q., Ionita, M., Kanzow, T., Wekerle, C., Rinke, A., 2023. Cyclones modulate the control of the North Atlantic Oscillation on transports into the Barents Sea. *Commun. Earth Environ.* 4, 324. <https://doi.org/10.1038/s43247-023-00985-1>
- Hofmann, Z., Von Appen, W., Kanzow, T., Becker, H., Hagemann, J., Hufnagel, L., Iversen, M.H., 2024. Stepwise Subduction Observed at a Front in the Marginal Ice Zone in Fram Strait. *J. Geophys. Res. Oceans* 129, e2023JC020641. <https://doi.org/10.1029/2023JC020641>
- Hofmann, Z., von Appen, W., Wekerle, C., 2021. Seasonal and Mesoscale Variability of the Two Atlantic Water Recirculation Pathways in Fram Strait. *J. Geophys. Res. Oceans*

- 126, 1–18. <https://doi.org/10.1029/2020JC017057>
- Holliday, N.P., Bersch, M., Berx, B., Chafik, L., Cunningham, S., Florindo-López, C., Hátún, H., Johns, W., Josey, S.A., Larsen, K.M.H., Mulet, S., Oltmanns, M., Reverdin, G., Rossby, T., Thierry, V., Valdimarsson, H., Yashayaev, I., 2020. Ocean circulation causes the largest freshening event for 120 years in eastern subpolar North Atlantic. *Nat. Commun.* 11, 585. <https://doi.org/10.1038/s41467-020-14474-y>
- Holliday, N.P., Hughes, S.L., Bacon, S., Beszczynska-Möller, A., Hansen, B., Lavín, A., Loeng, H., Mork, K.A., Østerhus, S., Sherwin, T., Walczowski, W., 2008. Reversal of the 1960s to 1990s freshening trend in the northeast North Atlantic and Nordic Seas. *Geophys. Res. Lett.* 35, L03614. <https://doi.org/10.1029/2007GL032675>
- Hoppmann, M., 2024. Collection of raw data from oceanographic moorings in the Fram Strait, Greenland Sea, and central Arctic Ocean, 2018–2025. <https://doi.pangaea.de/10.1594/PANGAEA.959812>
- Huang, B., Liu, C., Banzon, V., Freeman, E., Graham, G., Hankins, B., Smith, T., Zhang, H.-M., 2021. Improvements of the Daily Optimum Interpolation Sea Surface Temperature (DOISST) Version 2.1. *J. Clim.* 34, 2923–2939. <https://doi.org/10.1175/JCLI-D-20-0166.1>
- Huang, J., Pickart, R.S., Chen, Z., Huang, R.X., 2023. Role of air-sea heat flux on the transformation of Atlantic Water encircling the Nordic Seas. *Nat. Commun.* 14, 141. <https://doi.org/10.1038/s41467-023-35889-3>
- Ionita, M., Scholz, P., Lohmann, G., Dima, M., Prange, M., 2016. Linkages between atmospheric blocking, sea ice export through Fram Strait and the Atlantic Meridional Overturning Circulation. *Sci. Rep.* 6, 32881. <https://doi.org/10.1038/srep32881>
- Isachsen, P.E., LaCasce, J.H., Mauritzen, C., Häkkinen, S., 2003. Wind-Driven Variability of the Large-Scale Recirculating Flow in the Nordic Seas and Arctic Ocean. *J. Phys. Oceanogr.* 33, 2534–2550. [https://doi.org/10.1175/1520-0485\(2003\)033<2534:WVOTLR>2.0.CO;2](https://doi.org/10.1175/1520-0485(2003)033<2534:WVOTLR>2.0.CO;2)
- Isaksen, K., Nordli, Ø., Ivanov, B., Køltzow, M.A.Ø., Aaboe, S., Gjelten, H.M., Mezghani, A., Eastwood, S., Førland, E., Benestad, R.E., Hanssen-Bauer, I., Brækkan, R., Sviashchennikov, P., Demin, V., Revina, A., Karandasheva, T., 2022. Exceptional warming over the Barents area. *Sci. Rep.* 12, 9371. <https://doi.org/10.1038/s41598-022-13568-5>
- Jónsson, S., Foldvik, A., 1992. The transport and circulation in Fram Strait. *ICES. C.M.1992/C.10.* https://www.ices.dk/sites/pub/CM%20Documents/1992/C/1992_C10.pdf
- Karam, S., Heuzé, C., Hoppmann, M., De Steur, L., 2024. Continued warming of deep waters in the Fram Strait. *Ocean Sci.* 20, 917–930. <https://doi.org/10.5194/os-20-917-2024>
- Karcher, M.J., Gerdes, R., Kauker, F., Köberle, C., 2003. Arctic warming: Evolution and spreading of the 1990s warm event in the Nordic seas and the Arctic Ocean. *J. Geophys. Res. Oceans* 108, 2001JC001265. <https://doi.org/10.1029/2001JC001265>
- Kay, J.E., Holland, M.M., Jahn, A., 2011. Inter-annual to multi-decadal Arctic sea ice extent trends in a warming world. *Geophys. Res. Lett.* 38, 2011GL048008. <https://doi.org/10.1029/2011GL048008>
- Kim, S.-K., An, S.-I., 2024. Emergence of a climate oscillation in the Arctic Ocean due to global warming. *Nat. Clim. Change.* <https://doi.org/10.1038/s41558-024-02171-3>
- Körtke, W., Walter, M., Huhn, O., Kanzow, T., Rhein, M., 2024. Decadal Changes in the Pathways of the Atlantic Water Core in the Arctic Ocean Inferred From Transient Tracers. *J. Geophys. Res. Oceans* 129, e2024JC021419. <https://doi.org/10.1029/2024JC021419>
- L. Chafik, Nilsson, J., Skagseth, Ø., Lundberg, P., 2015. On the flow of Atlantic water and temperature anomalies in the Nordic Seas toward the Arctic Ocean. *J. Geophys. Res. Oceans* 120, 7897–7918. <https://doi.org/10.1002/2015JC011012>
- Long, Z., Perrie, W., Zhang, M., Liu, Y., 2024. Responses of Atlantic Water Inflow Through

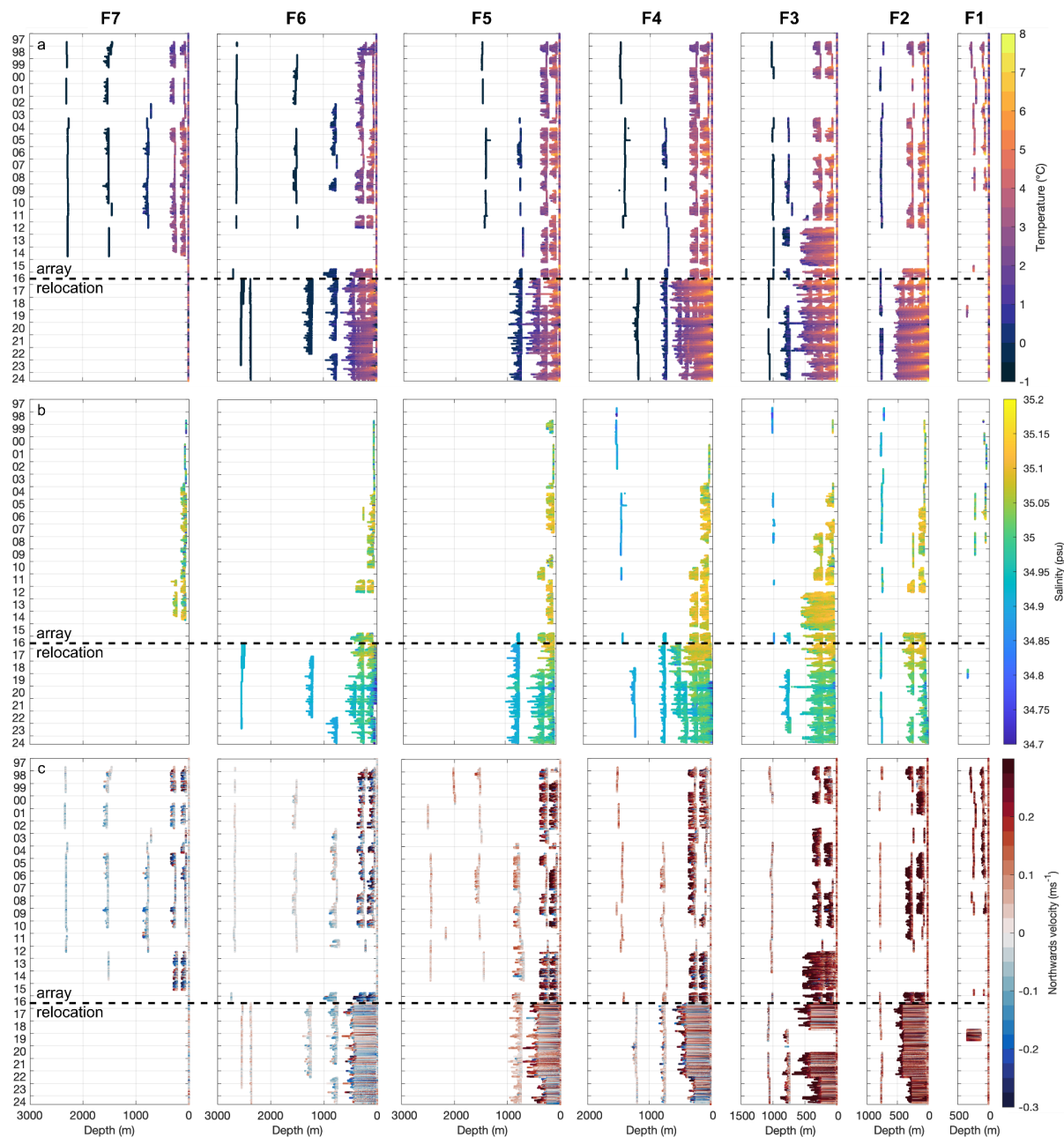
- Fram Strait to Arctic Storms. *Geophys. Res. Lett.* 51, e2023GL107777. <https://doi.org/10.1029/2023GL107777>
- Lundesgaard, Ø., Sundfjord, A., Renner, A.H.H., 2021. Drivers of Interannual Sea Ice Concentration Variability in the Atlantic Water Inflow Region North of Svalbard. *J. Geophys. Res. Oceans* 126, e2020JC016522. <https://doi.org/10.1029/2020JC016522>
- Marnela, M., Rudels, B., Houssais, M.-N., Beszczynska-Möller, A., Eriksson, P.B., 2013. Recirculation in the Fram Strait and transports of water in and north of the Fram Strait derived from CTD data. *Ocean Sci.* 9, 499–519. <https://doi.org/10.5194/os-9-499-2013>
- Mauritzen, C., Hansen, E., Andersson, M., Berx, B., Beszczynska-Möller, A., Burud, I., Christensen, K.H., Debernard, J., De Steur, L., Dodd, P., Gerland, S., Godøy, Ø., Hansen, B., Hudson, S., Høydalsvik, F., Ingvaldsen, R., Isachsen, P.E., Kasajima, Y., Koszalka, I., Kovacs, K.M., Køltzow, M., LaCasce, J., Lee, C.M., Lavergne, T., Lydersen, C., Nicolaus, M., Nilsen, F., Nøst, O.A., Orvik, K.A., Reigstad, M., Schyberg, H., Seuthe, L., Skagseth, Ø., Skarðhamar, J., Skogseth, R., Sperrevik, A., Svensen, C., Søiland, H., Teigen, S.H., Tverberg, V., Wexels Riser, C., 2011. Closing the loop – Approaches to monitoring the state of the Arctic Mediterranean during the International Polar Year 2007–2008. *Prog. Oceanogr.* 90, 62–89. <https://doi.org/10.1016/j.pocean.2011.02.010>
- McPherson, R.A., Wekerle, C., Kanzow, T., 2023. Shifts of the Recirculation Pathways in Central Fram Strait Drive Atlantic Intermediate Water Variability on Northeast Greenland Shelf. *J. Geophys. Res. Oceans* 128, e2023JC019915. <https://doi.org/10.1029/2023JC019915>
- McPherson, R.A., Wekerle, C., Kanzow, T., Ionita, M., Heukamp, F.O., Zeising, O., Humbert, A., 2024. Atmospheric blocking slows ocean-driven melting of Greenland's largest glacier tongue. *Science* 385, 1360–1366. <https://doi.org/10.1126/science.ado5008>
- Muijlwijk, M., Smedsrød, L.H., Ilicak, M., Drange, H., 2018. Atlantic Water Heat Transport Variability in the 20th Century Arctic Ocean From a Global Ocean Model and Observations. *J. Geophys. Res. Oceans* 123, 8159–8179. <https://doi.org/10.1029/2018JC014327>
- Nöthig, E.-M., Bracher, A., Engel, A., Metfies, K., Niehoff, B., Peek, I., Bauerfeind, E., Cherkasheva, A., Gäbler-Schwarz, S., Hardge, K., Kilias, E., Kraft, A., Mebrahtom Kidane, Y., Lalande, C., Piontek, J., Thomisch, K., Wurst, M., 2015. Summertime plankton ecology in Fram Strait—a compilation of long- and short-term observations. *Polar Res.* 34, 23349. <https://doi.org/10.3402/polar.v34.23349>
- Orvik, K.A., 2022. Long-Term Moored Current and Temperature Measurements of the Atlantic Inflow Into the Nordic Seas in the Norwegian Atlantic Current; 1995–2020. *Geophys. Res. Lett.* 49, e2021GL096427. <https://doi.org/10.1029/2021GL096427>
- Orvik, K.A., Niiler, P., 2002. Major pathways of Atlantic water in the northern North Atlantic and Nordic Seas toward Arctic. *Geophys. Res. Lett.* 29, 2-1-2–4. <https://doi.org/10.1029/2002GL015002>
- Park, J.-E., Kim, H.-C., Cho, K.-H., 2022. Variability of Near-Surface Salinity in the Nordic Seas Over the Past Three Decades (1991–2019). *Front. Mar. Sci.* 9, 969159. <https://doi.org/10.3389/fmars.2022.969159>
- Pérez-Hernández, M.D., Pickart, R.S., Torres, D.J., Bahr, F., Sundfjord, A., Ingvaldsen, R., Renner, A.H.H., Beszczynska-Möller, A., Von Appen, W., Pavlov, V., 2019. Structure, Transport, and Seasonality of the Atlantic Water Boundary Current North of Svalbard: Results From a Yearlong Mooring Array. *J. Geophys. Res. Oceans* 124, 1679–1698. <https://doi.org/10.1029/2018JC014759>
- Polyakov, I.V., Beszczynska, A., Carmack, E.C., Dmitrenko, I.A., Fahrbach, E., Frolov, I.E., Gerdes, R., Hansen, E., Holfort, J., Ivanov, V.V., Johnson, M.A., Karcher, M., Kauker, F., Morison, J., Orvik, K.A., Schauer, U., Simmons, H.L., Skagseth, Ø., Sokolov, V.T., Steele, M., Timokhov, L.A., Walsh, D., Walsh, J.E., 2005. One more step toward a warmer Arctic. *Geophys. Res. Lett.* 32, 2005GL023740. <https://doi.org/10.1029/2005GL023740>

- Polyakov, I.V., Ingvaldsen, R.B., Pnyushkov, A.V., Bhatt, U.S., Francis, J.A., Janout, M., Kwok, R., Skagseth, Ø., 2023. Fluctuating Atlantic inflows modulate Arctic atlantification. *Science* 381, 972–979. <https://doi.org/10.1126/science.adh5158>
- Polyakov, I.V., Pnyushkov, A.V., Alkire, M.B., Ashik, I.M., Baumann, T.M., Carmack, E.C., Gosczko, I., Guthrie, J., Ivanov, V.V., Kanzow, T., Krishfield, R., Kwok, R., Sundfjord, A., Morison, J., Rember, R., Yulin, A., 2017. Greater role for Atlantic inflows on sea-ice loss in the Eurasian Basin of the Arctic Ocean. *Science* 356, 285–291. <https://doi.org/10.1126/science.aai8204>
- Polyakov, I.V., Pnyushkov, A.V., Timokhov, L.A., 2012. Warming of the intermediate Atlantic water of the Arctic ocean in the 2000S. *J. Clim.* 25, 8362–8370. <https://doi.org/10.1175/JCLI-D-12-00266.1>
- Polyakov, I.V., Timokhov, L.A., Alexeev, V.A., Bacon, S., Dmitrenko, I.A., Fortier, L., Frolov, I.E., Gascard, J.-C., Hansen, E., Ivanov, V.V., Laxon, S., Mauritzen, C., Perovich, D., Shimada, K., Simmons, H.L., Sokolov, V.T., Steele, M., Toole, J., 2010. Arctic Ocean Warming Contributes to Reduced Polar Ice Cap. *J. Phys. Oceanogr.* 40, 2743–2756. <https://doi.org/10.1175/2010JPO4339.1>
- Quadfasel, D., Gascard, J.-C., Koltermann, K.-P., 1987. Large-scale oceanography in Fram Strait during the 1984 Marginal Ice Zone Experiment. *J. Geophys. Res.* 92, 6719. <https://doi.org/10.1029/JC092iC07p06719>
- Rantanen, M., Karpechko, A.Yu., Lippinen, A., Nordling, K., Hyvärinen, O., Ruosteenaja, K., Vihma, T., Laaksonen, A., 2022. The Arctic has warmed nearly four times faster than the globe since 1979. *Commun. Earth Environ.* 3, 168. <https://doi.org/10.1038/s43247-022-00498-3>
- Renner, A.H.H., Sundfjord, A., Janout, M.A., Ingvaldsen, R.B., Beszczynska-Möller, A., Pickart, R.S., Pérez-Hernández, M.D., 2018. Variability and Redistribution of Heat in the Atlantic Water Boundary Current North of Svalbard. *J. Geophys. Res. Oceans* 123, 6373–6391. <https://doi.org/10.1029/2018JC013814>
- Reynolds, R.W., Smith, T.M., Liu, C., Chelton, D.B., Casey, K.S., Schlax, M.G., 2007. Daily High-Resolution-Blended Analyses for Sea Surface Temperature. *J. Clim.* 20, 5473–5496. <https://doi.org/10.1175/2007JCLI1824.1>
- Rodionov, S.N., 2004. A sequential algorithm for testing climate regime shifts. *Geophys. Res. Lett.* 31, 2004GL019448. <https://doi.org/10.1029/2004GL019448>
- Rudels, B., 2010. Constraints on exchanges in the Arctic Mediterranean—do they exist and can they be of use? *Tellus Dyn. Meteorol. Oceanogr.* 62, 109. <https://doi.org/10.1111/j.1600-0870.2009.00425.x>
- Rudels, B., Meyer, R., Fahrbach, E., Ivanov, V.V., Østerhus, S., Quadfasel, D., Schauer, U., Tverberg, V., Woodgate, R.A., 2000. Water mass distribution in Fram Strait and over the Yermak Plateau in summer 1997. *Ann. Geophys.* 18, 687–705. <https://doi.org/10.1007/s00585-000-0687-5>
- Ruiz-Castillo, E., Janout, M., Hölemann, J., Kanzow, T., Schulz, K., Ivanov, V., 2023. Structure and Seasonal Variability of the Arctic Boundary Current North of Severnaya Zemlya. *J. Geophys. Res. Oceans* 128, e2022JC018677. <https://doi.org/10.1029/2022JC018677>
- Saes, M.J.M., Gjelstrup, C.V.B., Visser, A.W., Stedmon, C.A., 2022. Separating Annual, Interannual and Regional Change in Sea Surface Temperature in the Northeastern Atlantic and Nordic Seas. *J. Geophys. Res. Oceans* 127, e2022JC018630. <https://doi.org/10.1029/2022JC018630>
- Saloranta, T.M., Haugan, P.M., 2001. Interannual variability in the hydrography of Atlantic water northwest of Svalbard. *J. Geophys. Res. Oceans* 106, 13931–13943. <https://doi.org/10.1029/2000jc000478>
- Schauer, U., Beszczynska-Möller, A., Walczowski, W., Fahrbach, E., Piechura, J., Hansen, E., 2008. Variation of Measured Heat Flow Through the Fram Strait Between 1997 and 2006 BT - Arctic Subarctic Ocean Fluxes: Defining the Role of the Northern Seas in Climate. *Arctic–Subarctic Ocean Fluxes* 65–85.
- Schauer, U., Fahrbach, E., Osterhus, S., Rohardt, G., 2004. Arctic warming through the

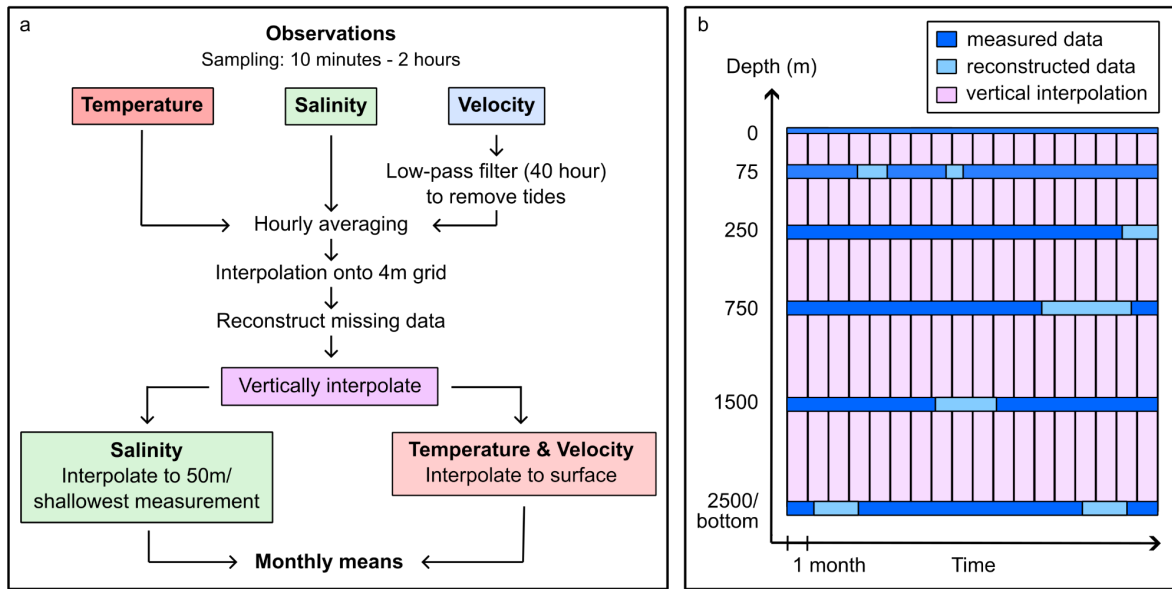
- Fram Strait: Oceanic heat transport from 3 years of measurements. *J. Geophys. Res. Oceans* 109, 2003JC001823. <https://doi.org/10.1029/2003JC001823>
- Schllichtholz, P., Houssais, M.-N., 2011. Forcing of oceanic heat anomalies by air-sea interactions in the Nordic Seas area. *J. Geophys. Res.* 116, C01006. <https://doi.org/10.1029/2009JC005944>
- Shi, W., Xu, M., Lv, X., 2024. Research on the change of the storage volume of the Nordic Seas Overflows over the last 40 years. *Front. Mar. Sci.* 11, 1302978. <https://doi.org/10.3389/fmars.2024.1302978>
- Shu, Q., Wang, Q., Árthun, M., Wang, S., Song, Z., Zhang, M., Qiao, F., 2022. Arctic Ocean Amplification in a warming climate in CMIP6 models. *Sci. Adv.* 8, eabn9755. <https://doi.org/10.1126/sciadv.abn9755>
- Skagseth, Ø., Orvik, K.A., Furevik, T., 2004. Coherent variability of the Norwegian Atlantic Slope Current derived from TOPEX/ERS altimeter data. *Geophys. Res. Lett.* 31, 2004GL020057. <https://doi.org/10.1029/2004GL020057>
- Smedsrød, L.H., Muilwijk, M., Brakstad, A., Madonna, E., Lauvset, S.K., Spensberger, C., Born, A., Eldevik, T., Drange, H., Jeansson, E., Li, C., Olsen, A., Skagseth, Ø., Slater, D.A., Straneo, F., Våge, K., Árthun, M., 2022. Nordic Seas Heat Loss, Atlantic Inflow, and Arctic Sea Ice Cover Over the Last Century. *Rev. Geophys.* 60. <https://doi.org/10.1029/2020RG000725>
- Soltwedel, T., Bauerfeind, E., Bergmann, M., Bracher, A., Budaeva, N., Busch, K., Cherkasheva, A., Fahl, K., Grzelak, K., Hasemann, C., Jacob, M., Kraft, A., Lalande, C., Metfies, K., Nöthig, E.-M., Meyer, K., Quéric, N.-V., Schewe, I., Włodarska-Kowalczuk, M., Klages, M., 2016. Natural variability or anthropogenically-induced variation? Insights from 15 years of multidisciplinary observations at the arctic marine LTER site HAUSGARTEN. *Ecol. Indic.* 65, 89–102. <https://doi.org/10.1016/j.ecolind.2015.10.001>
- Straneo, F., Heimbach, P., 2013. North Atlantic warming and the retreat of Greenland's outlet glaciers. *Nature* 504, 36–43. <https://doi.org/10.1038/nature12854>
- Straneo, F., Sutherland, D.A., Holland, D., Gladish, C., Hamilton, G.S., Johnson, H.L., Rignot, E., Xu, Y., Koppes, M., 2012. Characteristics of ocean waters reaching Greenland's glaciers. *Ann. Glaciol.* 53, 202–210. <https://doi.org/10.3189/2012AoG60A059>
- Tsubouchi, T., Våge, K., Hansen, B., Larsen, K.M.H., Østerhus, S., Johnson, C., Jónsson, S., Valdimarsson, H., 2021. Increased ocean heat transport into the Nordic Seas and Arctic Ocean over the period 1993–2016. *Nat. Clim. Change* 11, 21–26. <https://doi.org/10.1038/s41558-020-00941-3>
- Tsubouchi, T., Von Appen, W.-J., Kanzow, T., De Steur, L., 2023. Temporal variability of the overturning circulation in the Arctic Ocean and the associated heat and freshwater transports during 2004–2010. *J. Phys. Oceanogr.* <https://doi.org/10.1175/JPO-D-23-0056.1>
- Voet, G., Quadfasel, D., Mork, K.A., Søiland, H., 2010. The mid-depth circulation of the Nordic Seas derived from profiling float observations. *Tellus A* 62, 516–529. <https://doi.org/10.1111/j.1600-0870.2010.00444.x>
- Volkov, D.L., Pujol, M. -Isabelle, 2012. Quality assessment of a satellite altimetry data product in the Nordic, Barents, and Kara seas. *J. Geophys. Res. Oceans* 117, 2011JC007557. <https://doi.org/10.1029/2011JC007557>
- von Appen, W.-J., 2019. Physical oceanography and current meter data (including raw data) from FRAM moorings in the Fram Strait, 2016–2018. <https://doi.org/10.1594/PANGAEA.904565>
- von Appen, W.-J., Beszczynska-Möller, A., Schauer, U., Fahrbach, E., 2019. Physical oceanography and current meter data from moorings F1-F14 and F15/F16 in the Fram Strait, 1997–2016. <https://doi.org/10.1594/PANGAEA.900883>
- von Appen, W.-J., Schauer, U., Hattermann, T., Beszczynska-Möller, A., 2016. Seasonal Cycle of Mesoscale Instability of the West Spitsbergen Current. *J. Phys. Oceanogr.* 46, 1231–1254. <https://doi.org/10.1175/JPO-D-15-0184.1>

- von Appen, W.-J., Schauer, U., Somavilla, R., Bauerfeind, E., Beszczynska-Möller, A., 2015. Exchange of warming deep waters across Fram Strait. Deep Sea Res. Part Oceanogr. Res. Pap. 103, 86–100. <https://doi.org/10.1016/j.dsr.2015.06.003>
- von Appen, W.-J., Waite, A.M., Bergmann, M., Bienhold, C., Boebel, O., Bracher, A., Cisewski, B., Hagemann, J., Hoppema, M., Iversen, M.H., Konrad, C., Krumpen, T., Lochthofen, N., Metfies, K., Niehoff, B., Nöthig, E.M., Purser, A., Salter, I., Schaber, M., Scholz, D., Soltwedel, T., Torres-Valdes, S., Wekerle, C., Wenzhöfer, F., Wietz, M., Boetius, A., 2021. Sea-ice derived meltwater stratification slows the biological carbon pump: results from continuous observations. Nat. Commun. 12. <https://doi.org/10.1038/s41467-021-26943-z>
- Wang, Q., Shu, Q., Wang, S., Beszczynska-Moeller, A., Danilov, S., Steur, L., Haine, T.W.N., Karcher, M., Lee, C.M., Myers, P.G., Polyakov, I.V., Provost, C., Skagseth, Ø., Spreeen, G., Woodgate, R., 2023. A Review of Arctic–Subarctic Ocean Linkages: Past Changes, Mechanisms, and Future Projections. Ocean-Land-Atmosphere Res. 2, 0013. <https://doi.org/10.34133/olar.0013>
- Wang, Q., Wekerle, C., Wang, X., Danilov, S., Koldunov, N., Sein, D., Sidorenko, D., Appen, W., Jung, T., 2020. Intensification of the Atlantic Water Supply to the Arctic Ocean Through Fram Strait Induced by Arctic Sea Ice Decline. Geophys. Res. Lett. 47. <https://doi.org/10.1029/2019GL086682>
- Wekerle, C., McPherson, R. A., Von Appen, W.-J., Wang, Q., Timmermann, R., Scholz, P., Danilov, S., Shu, Q., Kanzow, T., 2024. Atlantic Water warming increases melt below Northeast Greenland's last floating ice tongue. Nat. Commun. 15, 1336. <https://doi.org/10.1038/s41467-024-45650-z>
- Zeising, O., Neckel, N., Dörr, N., Helm, V., Steinhage, D., Timmermann, R., Humbert, A., 2024. Extreme melting at Greenland's largest floating ice tongue. The Cryosphere 18, 1333–1357. <https://doi.org/10.5194/tc-18-1333-2024>

Supplementary Figures

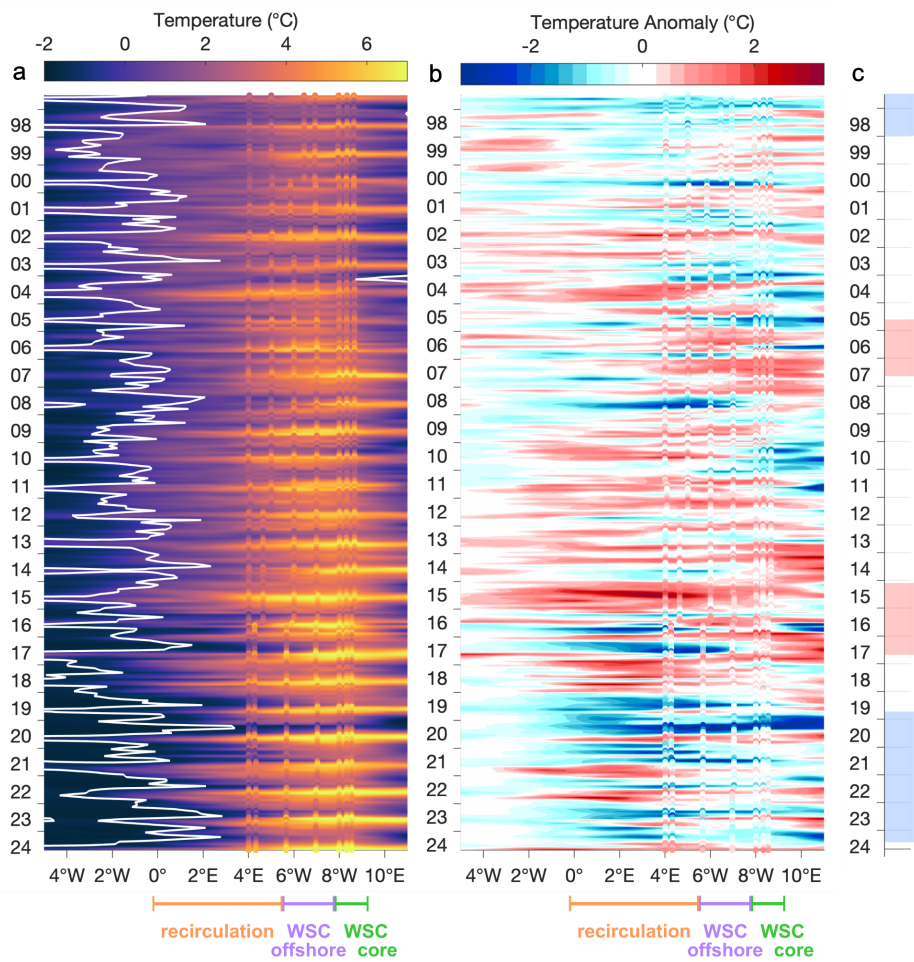


Supplementary Figure 1. Summary of original data measured at each WSC mooring location. Original data from each mooring across the WSC array, showing (a) temperature, (b) salinity, and (c) northwards velocity at sites F1 to F7 (labelled). Surface data are from satellite observations. The horizontal dashed line marks July 2016, when the mooring array was relocated northwards from $78^{\circ}50'\text{N}$ to 79°N .

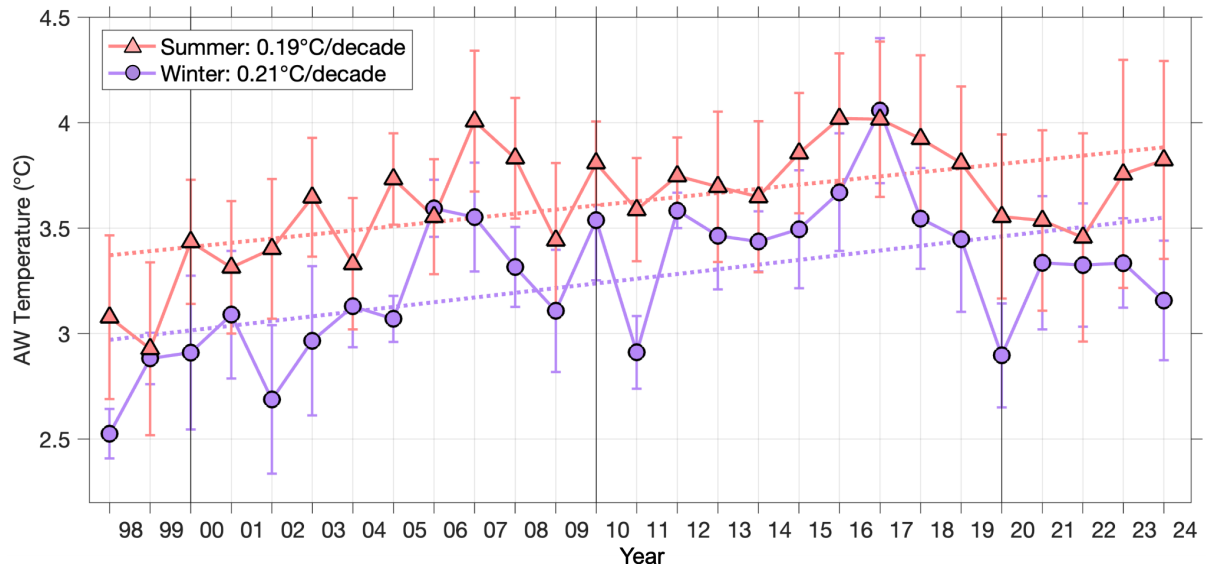


Supplementary Figure 2: Simplified schematic of mooring data processing. (a)

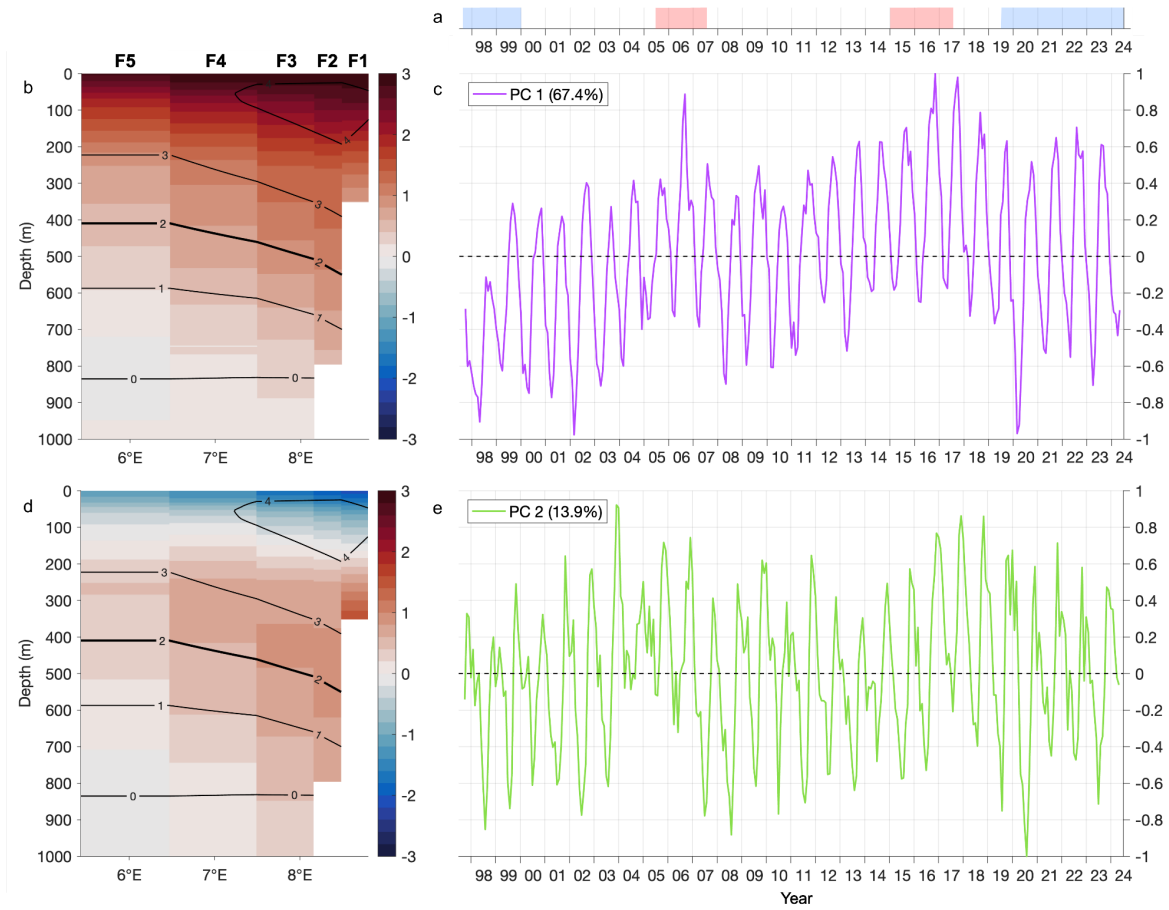
Flowchart outlining the key steps used to construct the gridded fields of temperature, salinity and velocity from the mooring array and used in this analysis. (b) Schematic illustration of the data reconstruction process, showing how data gaps were filled by reconstructed data at the nominal depths, followed by vertical interpolation and monthly averaging.



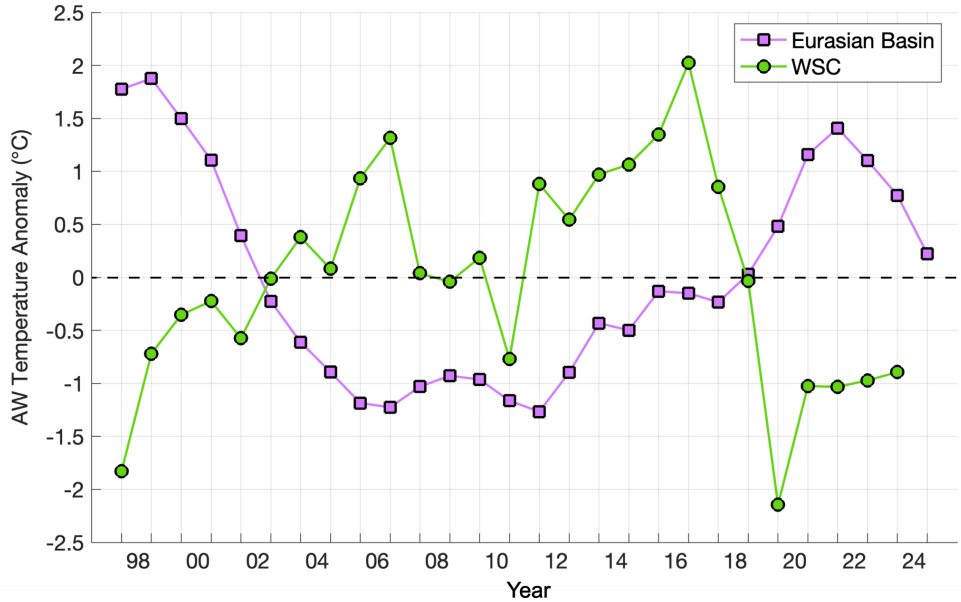
Supplementary Figure 3. Spatio-temporal variability of sea surface temperature across Fram Strait. Hovmöller diagrams of (a) monthly mean sea surface temperature, and (b) temperature anomalies, with the long-term trend and seasonal cycle removed. (c) The warm (red) and cold (blue) AW temperature anomalies, as defined in Fig. 5d. In (a), the white contour indicates the mean sea ice edge, defined by the 50% ice concentration. Superimposed on (a) and (b) are the corresponding mooring-derived upper ocean temperatures, averaged over the upper 75 m.



Supplementary Figure 4. Seasonal variability of Atlantic Water temperatures in the WSC. Timeseries of the Atlantic Water (AW) temperatures across the WSC (F1 - F5) are shown for winter (DJF), and summer (JJA), with whiskers representing the standard deviation. Linear trends for each season are indicated by dashed lines and included in the legend. Vertical lines mark the start of each decade.



Supplementary Figure 5. EOFs of AW temperature variability in the WSC. (a) Timing of the warm (red) and cold (blue) AW temperature anomalies, as defined in Fig. 5d. The first two EOFs of the monthly AW temperature across moorings F1 - F5. Maps in (a,c) show the spatial distribution, and (b,d) are the corresponding principal components. The timeseries have been normalised such that the amplitude of the nodes is contained in the maps. Selected mean isotherms are the black contours in the maps; the thick black line represents the mean depth of the AW layer (2°C isotherm). This figure is analogous to Fig. 9 but incorporates the seasonal cycle.



Supplementary Figure 6: Downstream advection of AW temperature anomalies.

Comparison of annual AW temperature anomalies in the WSC core (green) and the Eurasian Basin (purple) from 1997 - 2025. Both timeseries have been detrended and normalised. The Eurasian Basin data is from ORAS5 ocean reanalysis (Copernicus Climate Change Service, 2021) which has a horizontal resolution of $0.25^\circ \times 0.25^\circ$ (~ 9 km in the Arctic). The Eurasian Basin region is defined between $82 - 87^\circ\text{N}$, $95^\circ 30'\text{E} - 137^\circ\text{E}$. AW is defined as water temperatures $> 0^\circ\text{C}$, averaged over the upper 500 m.

Supplementary Tables

Mooring	F7	F6	F5	F4	F3	F2	F1
Longitude (°E)	4	4.79	5.96	7	8	8.33	8.65
Temperature (°C)							
Depth (m)							
75	3.34 ± 1.03	3.30 ± 1.14	3.75 ± 1.04	4.14 ± 1.11	4.42 ± 1.16	4.49 ± 1.25	4.47 ± 1.39
250	2.80 ± 0.64	2.71 ± 0.65	2.90 ± 0.62	3.29 ± 0.69	3.57 ± 0.73	3.75 ± 0.71	3.69 ± 0.70
750	-0.05 ± 0.17	0.05 ± 0.22	0.12 ± 0.40	0.27 ± 0.58	0.38 ± 0.61	0.61 ± 0.85	-
1500	-0.69 ± 0.07	-0.65 ± 0.12	-0.69 ± 0.10	-0.87 ± 0.04	-	-	-
2500	-0.78 ± 0.07	-0.77 ± 0.05	-	-	-	-	-
Velocity (ms⁻¹)							
Depth (m)							
75	-0.03 ± 0.10	-0.01 ± 0.11	0.05 ± 0.11	0.05 ± 0.12	0.14 ± 0.11	0.18 ± 0.12	0.19 ± 0.08
250	-0.03 ± 0.08	-0.01 ± 0.09	0.04 ± 0.10	0.05 ± 0.12	0.14 ± 0.11	0.18 ± 0.11	0.19 ± 0.08
750	-0.03 ± 0.04	-0.02 ± 0.04	0.02 ± 0.04	0.04 ± 0.06	0.06 ± 0.05	0.09 ± 0.07	-
1500	-0.05 ± 0.03	-0.01 ± 0.02	0.02 ± 0.04	0.08 ± 0.06	-	-	-
2500	-0.06 ± 0.04	0.0 ± 0.04	0.03 ± 0.03	-	-	-	-

Supplementary Table 1. Summary of statistics for each mooring. Long-term mean ± standard deviation of observed temperature and northwards velocity at nominal depths for moorings F1 (east) through F7 (west), covering the period from September 1997 - August 2024. Standard deviations are calculated from the monthly mean values. Depths without instruments at any time are omitted. Mean values correspond to those shown in Figure 3.

	1997 - 2016	2016 - 2024	1997 - 2016	2016 - 2024	1997 - 2016	2016 - 2024	1997 - 2016	2016 - 2024	1997 - 2016	2016 - 2024	1997 - 2016	2016 - 2024	1997 - 2016	2016 - 2024
Mooring	F7		F6		F5		F4		F3		F2		F1	
Lon (°E)	4.02	-	4.94	4.29	6.07	5.67	6.98	7.00	7.99	8.00	8.33	8.33	8.66	8.52
Temperature (°C)														
75m	3.13 ± 1.15	-	3.32 ± 1.25	3.31 ± 1.23	3.74 ± 1.05	3.85 ± 1.23	4.09 ± 1.10	4.34 ± 1.21	4.36 ± 1.13	4.62 ± 1.33	4.36 ± 1.30	4.64 ± 1.26	3.94 ± 1.61	-
250m	2.59 ± 0.69	-	2.60 ± 0.76	2.93 ± 0.61	2.91 ± 0.73	2.89 ± 0.59	3.22 ± 0.69	3.49 ± 0.74	3.52 ± 0.74	3.79 ± 0.86	3.70 ± 0.71	3.89 ± 0.84	3.34 ± 0.76	3.44 ± 0.92
750m	-0.03 ± 0.26	-	0.02 ± 0.34	0.12 ± 0.29	0.16 ± 0.56	0.18 ± 0.44	0.30 ± 0.78	0.26 ± 0.60	0.36 ± 0.84	0.53 ± 0.77	0.62 ± 0.98	0.61 ± 0.95	-	-
1500m	-0.72 ± 0.06	-	-0.70 ± 0.05	-0.47 ± 0.05	-0.76 ± 0.07	-	-0.88 ± 0.04	-0.81 ± 0.01	-	-	-	-	-	-
2500m	-0.86 ± 0.03	-	-0.81 ± 0.05	-0.72 ± 0.01	-	-	-	-	-	-	-	-	-	-
Velocity (ms⁻¹)														
75m	-0.02 ± 0.14	-	-0.01 ± 0.14	-0.01 ± 0.12	0.05 ± 0.13	0.05 ± 0.14	0.06 ± 0.14	0.05 ± 0.16	0.13 ± 0.15	0.16 ± 0.15	0.18 ± 0.14	0.17 ± 0.14	0.18 ± 0.12	-
250m	-0.02 ± 0.11	-	-0.01 ± 0.10	-0.01 ± 0.11	0.04 ± 0.11	0.05 ± 0.12	0.06 ± 0.11	0.04 ± 0.14	0.14 ± 0.13	0.15 ± 0.14	0.18 ± 0.12	0.19 ± 0.14	0.22 ± 0.10	0.19 ± 0.12
750m	-0.03 ± 0.06	-	-0.01 ± 0.05	-0.02 ± 0.05	0.01 ± 0.06	0.02 ± 0.04	0.04 ± 0.06	0.01 ± 0.07	-	0.04 ± 0.11	0.09 ± 0.08	0.10 ± 0.10	-	-
1500m	-0.04 ± 0.05	-	-0.01 ± 0.03	0.0 ± 0.08	0.03 ± 0.05	-	0.09 ± 0.06	0.05 ± 0.06	-	-	-	-	-	-
2500m	-0.05 ± 0.05	-	-0.01 ± 0.04	0.02 ± 0.05	0.04 ± 0.05	-	-	-	-	-	-	-	-	-

Supplementary Table 2. Summary of statistics for each mooring at both latitudes. Long-term mean \pm standard deviation of observed temperature and northward velocity at nominal depths for moorings F1 (east) through F7 (west), at both mooring locations. The left-hand column is when the moorings were positioned at 78°50'N (July 1997 - July 2016) and the right-hand column is at 79°N (July 2016 - August 2024) (see Figure 2a). Standard deviations are calculated from the monthly mean values. Depths without instruments at any time are omitted.

Year	1998	1999	2000	2001	2002	2003	2004	2005	2006	2007	2008	2009	2010	2011
Temperature (°C)														
Core	2.83 ± 0.40	3.11 ± 0.25	3.22 ± 0.57	3.27 ± 0.58	3.22 ± 0.53	3.37 ± 0.59	3.49 ± 0.35	3.44 ± 0.38	3.66 ± 0.39	3.78 ± 0.59	3.51 ± 0.60	3.51 ± 0.46	3.59 ± 0.55	3.40 ± 0.48
Offshore	2.56 ± 0.40	2.82 ± 0.27	2.99 ± 0.46	2.98 ± 0.41	2.83 ± 0.56	3.01 ± 0.58	3.02 ± 0.26	3.21 ± 0.37	3.43 ± 0.29	3.53 ± 0.43	3.22 ± 0.48	3.14 ± 0.36	3.28 ± 0.42	3.12 ± 0.42
Total	2.72 ± 0.40	3.00 ± 0.26	3.13 ± 0.52	3.16 ± 0.51	3.06 ± 0.54	3.23 ± 0.58	3.30 ± 0.31	3.35 ± 0.38	3.57 ± 0.35	3.68 ± 0.53	3.39 ± 0.56	3.36 ± 0.42	3.47 ± 0.50	3.28 ± 0.45
Year	2012	2013	2014	2015	2016	2017	2018	2019	2020	2021	2022	2023	2024	
Temperature (°C)														
Core	3.80 ± 0.40	3.75 ± 0.54	3.87 ± 0.47	3.92 ± 0.46	4.00 ± 0.50	4.18 ± 0.66	3.94 ± 0.65	3.76 ± 0.62	3.30 ± 0.77	3.58 ± 0.64	3.61 ± 0.62	3.65 ± 0.70	3.69 ± 0.63	
Offshore	3.32 ± 0.29	3.16 ± 0.49	3.23 ± 0.30	3.30 ± 0.28	3.46 ± 0.34	3.58 ± 0.48	3.44 ± 0.48	3.30 ± 0.46	3.03 ± 0.60	3.10 ± 0.45	3.22 ± 0.44	3.19 ± 54	3.19 ± 0.44	
Total	3.61 ± 0.36	3.51 ± 0.52	3.61 ± 0.40	3.67 ± 0.39	3.79 ± 0.43	3.94 ± 0.59	3.74 ± 0.58	3.58 ± 0.55	3.19 ± 0.70	3.39 ± 0.57	3.45 ± 0.55	3.46 ± 0.64	3.49 ± 0.56	

Supplementary Table 3: Mean AW temperatures of the WSC. Annual mean ± standard deviation of AW temperature for the WSC core, offshore branch, and combined WSC. Standard deviations are calculated from the monthly mean values. The values (and colours) correspond to the three timeseries shown in Figure 7.

Year	1969	1970	1971	1972	1973	1974	1975	1976	1977	1978	1979
Temperature (°C)	4.1	4.5	4.3	4.0	3.9	3.8	3.2	3.6	2.8	3.0	3.3
Year	1980	1981	1982	1983	1984	1985	1986	1987	1988	1989	
Temperature (°C)		3.2	3.4	3.2	4.2	4.1	3.6	3.2	2.9	3.1	3.6
Year	1990	1991	1992	1993	1994	1995	1996	1997			
Temperature (°C)		4.2	4.6	4.9	4.6	4.2	3.2	3.7	3.8		

Supplementary Table 4: Historical CTD data of the WSC. Annual mean temperature from CTD surveys between 1969 and 1997 over the onshore branch of the WSC, spanning the 300 - 1200 m isobaths and latitudes from 78° 50'N – 79° 30'N. Values are then averaged over the 100 - 300 m depth range. These data correspond to Figure 4a in Salaranta and Haugan (2001), and were used in Figure 11 in this study, with a seasonal offset applied (see Methods).